TECHNISCHE UNIVERSITÄT WIEN
Vienna | Austria

Diplomarbeit

Characterisation of the spin-dependent detector for the Ramsey GRS

zur Erlangung des akademischen Grades

Diplom-Ingenieur

an der

Technische Universität Wien

ausgeführt am
Atominstitut der Technische Universität Wien
Stadionallee 2
1020 Wien

unter der Anleitung von
Univ. Prof. Dipl.-Phys. Dr.rer.nat. Hartmut Abele

eingereicht von
Hugo Wetter
n11832655

Ort, Datum

Unterschrift (Studierender)

Contents

1 Introduction **1**
1.1 The qBounce experiment 1
1.2 Theory of the Gravity Resonance Spectroscopy 2
1.2.1 Ultra-Cold Neutrons 3
1.2.2 The Ramsey method of oscillating fields 3
1.3 Spin polarisation and detection 10

2 Polarisation and spin-flip theory **12**
2.1 Relations between the expected detection rates and the polarisation efficiency 12
2.2 Spin-flip and Larmor frequency 15

3 The Test-Beam experiment **18**
3.1 Working principle 18
3.1.1 Needs of the experiment 18
3.1.2 Protocol for different measurements 19
3.2 Description of the setup 20
3.2.1 Characterisation of the detector 21
3.2.2 Description of the whole installation 24

4 Data analysis and interpretation **30**
4.1 Data treatment and computation 30
4.2 Polarisation efficiency 33
4.3 Spin-flip efficiency 38

A Measurement of the mirror steps **42**

Kurzfassung

In den letzten Jahren erlebten Schwerkraftversuche aus mehreren Gründen eine Renaissance: Moderne astronomische Beobachtungen weisen eindeutig auf die Existenz von dunkler Energie und dunkler Materie hin. Ihre wahre Natur und ihr Inhalt bleiben jedoch ein Rätsel. Darüber hinaus erfordern prominente Kandidaten für die Formulierung einer konsistenten Quantentheorie der Gravitation zusätzliche räumliche Dimensionen. Das Neutron ist ein ideales Werkzeug zur Beantwortung solcher Fragen. Genauer gesagt ermöglichen gebundene Quantenzustände ultrakalter Neutronen im Schwerefeld der Erde die Kombination von Gravitationsexperimenten auf kurze Distanz mit leistungsstarken Resonanzspektroskopietechniken.

Neuere theoretische Entwicklungen legen nahe, dass eine genaue Bestimmung der Übergangsfrequenzen zwischen Gravitationsquantenzuständen in zusätzlichen Magnetfeldern und eine polarisationsabhängige Analyse es ermöglichen, das Konzept der Torsion in der Allgemeinen Relativitätstheorie zu testen. Daher haben wir als logische Fortsetzung der laufenden experimentellen qBounce-Kampagne Magnetfelder in das vorhandene Setup implementiert.

Unsere Arbeit war hauptsächlich ein Test von Polarisierungstechniken und eine Bestimmung ihrer Effizienz. Wir haben ein Nebenexperiment aufgebaut, in dem wir einen Polarisator innerhalb ein Hältefeld benützt haben, um die Neutronen nach Spin zu filtern. Wir haben auch einen Detektor hinzugefügt, der auch als Analysator benützt werden kann, damit ausschließlich die Neutronen mit dem richtigen Spin durchgehen können.

Um die Polarisationseffizienz zu messen, wir haben $Spin{-}flippers$ benützt. Sie sind magnetische Geräte, die die Fähigkeit haben, die Spinrichtung der durchgehenden Teilchen zu invertieren.

Abstract

In recent years, gravity experiments have been experiencing a renaissance for several reasons: Modern astronomical observations clearly point to the existence of dark energy and dark matter. Their true nature and content remain a mystery, however. Furthermore, prominent candidates for formulating a consistent quantum theory of gravitation require extra spatial dimensions. The neutron is an ideal tool for answering such questions. More precisely, bound quantum states of ultra-cold neutrons in the Earth's gravity field make it possible to combine gravity experiments at short distances with powerful resonance spectroscopy techniques.

Recent theoretical developments suggest that a precise determination of the transition frequencies between gravitational quantum states in additional magnetic fields and polarization-dependent analysis allows to test the concept of torsion in General Relativity. Therefore, as a logical continuation of the ongoing qBounce experimental campaign, we implemented magnetic fields inside the existing setup.

Our work was focused on the polarization techniques and the evaluation of their efficiency. We built a side-experiment setup in which we used a polarizer within a guiding magnetic field to sort the neutrons by spin, and a detector which can also be used as an analyser for the right spin-direction to come through.

In order to measure the polarization-efficiency, we used spin-flippers. They are magnetic devices able to invert the spin-direction of the particles passing through it.

Chapter 1

Introduction

This chapter presents key-elements of the qBounce experiment. It starts with a description of the qBounce setup. The second part of the chapter is a theoretical approach of the Ramsey method for GRS (standing for Gravity Resonance Spectroscopy, a frequency measurement made on particles brought to an excited state using gravity). It comes along with a description on how the wave functions of the Ultra-Cold Neutrons (much slower neutrons than thermic neutrons, see 1.2.1) behave when passing onto consecutive mirrors, an essential issue for this particular setup. The third section will deal with the polarization of the neutrons and its relevance for the qBounce experiment. After a short reminder of the principles of polarization, we will introduce the side experiment to qBounce that we lead and what we hoped to learn from it.

1.1 The qBounce experiment

The gravitational resonance technique formerly used by qBounce was the Rabi method, used for the testing of Newton's Law of Gravity [Jenke et al.14; Jenke11] and searches for hypothetical gravity-like interactions. This method implies either a mechanical oscillation or an oscillating magnetic gradient. The setup includes two selecting mirrors at both ends of the neutron path, with rough mirrors above them. They are called state selectors because neutrons in higher excited states are discarded by the rough mirror, called an *absorber*, and only neutrons in the lower states remain. The absorber is adjustable and can be set so that only the ground state or the first few excited states remain. For the Rabi method, there used to be a single perturbation region finding itself in the middle. The perturbation region is a mirror that neutrons go past while being brought an energetic perturbation. qBounce carries out this method with an oscillating mirror for mechanical perturbations. The method currently in use is the Ramsey method, which consists in a splitting of the perturbation region in two distinct regions. In the case of the Ramsey method, two oscillating mirrors sit separated by a longer static mirror, called the free-propagation region. They are still surrounded by selecting mirrors, indispensable to sort the neutrons by states.

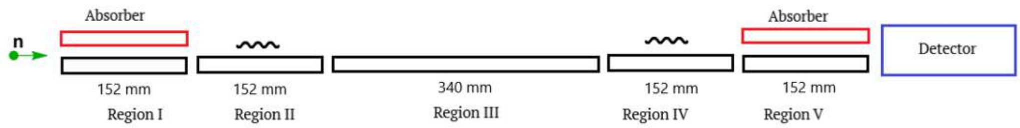

Figure 1.1: Side view of the schematic qBounce setup

In qBounce, mechanical oscillations are being used to trigger the state excitation of the neutrons, symbolized by the waves on the drawing. Brass spacers are used to lock the absorbers on the mirrors for regions I and V, with the possibility to adjust their relative height, depending on the states we want to admit.

The mirrors are stabilised with the help of piezoelectric sensors. They all must be at the same height at rest, and without any angle. A further study concerning this point has been lead and is displayed in the appendix A.

1.2 Theory of the Gravity Resonance Spectroscopy

We can define Gravitational Resonance Spectroscopy as the frequency measurements that can be made by sending particles (in our case, neutrons) on a hard surface under the gravitational field. Under the potential gradient caused by gravity, neutrons adopt discrete states, called bound states. The process of oscillating perturbation induces discrete quantum transitions with resonance between these bound states. With a state selector, the energy spectrum of the excited neutrons can thus be measured by comparing the rates of incoming particles when the selector is used and when it is not. The qBounce experiment performs energetic transitions of such neutrons with the help of oscillating mirrors to analyse their behaviour. Eventually, a goal is to look for evidence whether there may exist a Non-Newtonian form of gravity. With its high precision, this experiment could perform this investigation on the micrometer scale, especially thanks to the use of a Ultra-Cold Neutrons detector based on a ^{10}B converter.

1.2.1 Ultra-Cold Neutrons

The Laue-Langevin Institute (ILL) has the ability to produce ultra-cold neutrons (commonly refered to as UCN). UCN are neutrons defined by their maximal velocity. With a pragmatic definition, UCN are neutrons which are reflected under any angle of incidence on surfaces and can be stored without interacting with their container. The ILL owns a neutron High-Flux Reactor able to produce a continuous neutron flux with an intensity of 1.5×10^{15} n/s/cm^2 (n is the number of neutrons) and a power of 58.3 MW. These performances make the neutron reactor of the ILL unique around the world. The generation process of UCN is rather complex: the neutrons produced by the reactor are "cooled" in a bath of heavy water (D_2O). They follow a neutron guide upwards, so that their kinetic energy is converted into potential energy; at the ultra-cold neutrons beam facility, called PF2, they travel through a turbine [Phillips98], which takes out their forward velocity down to about 10 m/s. They fill the neutron guides in a so-called "steady-flow mode", making them ready to use.

They are used for several scientific experiments in various realms of study, like the measurement of the neutron lifetime or the search for an electric dipole-moment [Pokotilovski18]. The spectroscopic measuring methods are themselves broadly used in experimental science. PF2 is a group of platforms of the ILL, including "UCN", which has been now dedicated to GRS for several years, and is at the time at the disposal of qBounce. At the exit, just in front of our experiment, the values of the neutron velocity are between 3 m/s and 15 m/s with a most probable velocity at around 11 m/s.

1.2.2 The Ramsey method of oscillating fields

The Rabi and Ramsey methods are widely used to study atomic transitions, magnetic moments, clocks, and thus many experimental ends need either of them for spectroscopy, including Nuclear Magnetic Resonance in medicine.

Their overall principle is a state transition between two discrete quantum states through field oscillations, in order to determine the transition frequency between the studied states.

Some experiments revolving around these methods use a beam of particles and drive a transition by using a time-dependent magnetic field acting along the perturbation region(s). In the case of qBounce, oscillating mirrors are used to create perturbations and provide transitions between quantum states in the gravity potential. Regarding the Rabi spectroscopy, particles should all have equal velocities, because the effect of the perturbations on a particle depends on the time that this particles spends under the perturbation. It means that disparate velocities will lead to imprecise measurements. This is not the case for Ramsey-spectroscopy, see next paragraph.

Consider a two-state system including $|0\rangle$ and $|1\rangle$: it can be represented by an arrow in the Bloch-Sphere of which poles are the pure states $|0\rangle$ and $|1\rangle$. Under perturbation, particles may switch from the state $|0\rangle$ to the state $|1\rangle$, which is visualized on the Bloch-Sphere by a rotation of the arrow. A transition from a pure state to the other is a rotation of half a turn, and we call it a π-flip. Though the Rabi method uses a single oscillating mirror which performs a π-flip on the neutrons, allowing in principle a homogeneous energetic transition between the studied eigenstates, the Ramsey method involves two separate and short interaction zones, each performing a $\pi/2$-flip to the neutrons. A $\pi/2$-flip leaves the system to any state perpendicular to one of the initial states on the sphere. The Rabi method is especially limited by the width of the speed distribution and by the imperfections of the mechanical oscillations. Indeed, the neutrons will experience different interacting times and thus behave differently. These limitations are all the greater as the oscillating region is long. The Ramsey method attenuates this flaw by a significant extent by involving two smaller interaction regions separated by a static region. The middle region allows therefore free propagation of the particles before they reach the second interaction region. Norman Ramsey has shown in [Ramsey50] that the separation of the regions increases the accuracy by sharpening the resonance peak, allowing the perturbation frequency to be more precisely approached.

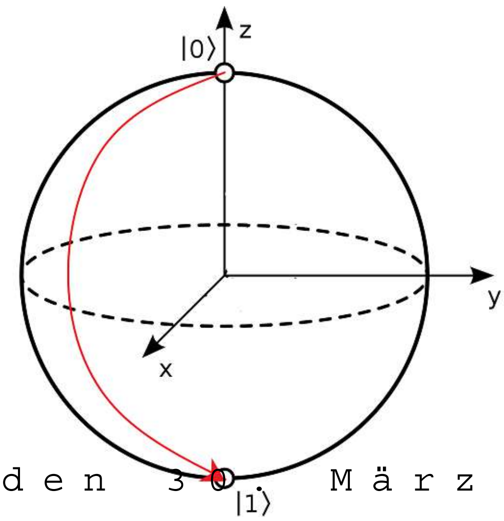

Figure 1.2: π-flip (red arrow) from the pure state $|0\rangle$ to the state $|1\rangle$

In the terrestrial frame of reference, a UCN is a quantum particle ruled

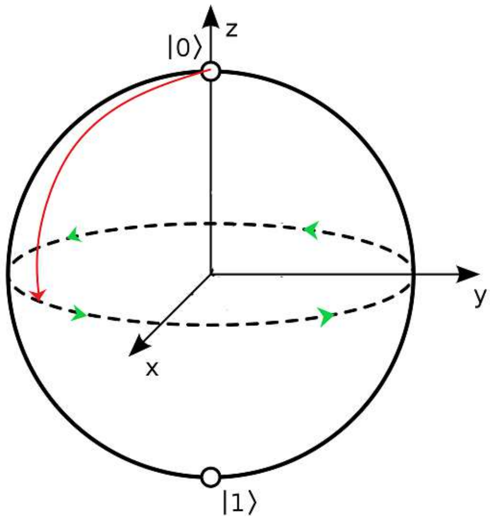

Figure 1.3: $\pi/2$-flip (red arrow) from the pure state $|0\rangle$ to a mixed state and free propagation (green arrows)

by the Schrödinger equation under the gravity potential mgz proportional to its own height z, with m the mass of the neutron and g the local gravity acceleration of the Earth. We define z so that the level of the mirror is at $z = 0$. This reads, in the position space:

$$i\hbar \frac{d\psi(\vec{r},t)}{dt} = (\frac{-\hbar^2}{2m}\Delta + mgz + \hat{V}(z))\psi(\vec{r},t) \tag{1.1}$$

The first term of the Hamiltonian is the kinetic energy given by the Laplace operator Δ. For a neutron, $m \approx 939.57$ MeV/c^2. Its potential energy is the sum of its gravitational potential and the optical potential of the mirror, which is equal to 0 for a positive height and to the potential $\hat{V_0}$ for a negative height. It is therefore given by $\hat{V}(z) = \hat{V_0}\Theta(-z)$ with Θ the Heaviside step function.

We write the time-independent Schrödinger equation to describe and study the eigenstates corresponding to the time-independent Hamilton operator. Be $n \in \mathbb{N}$; the eigenstate ψ_n follows the equation:

$$\hat{H}\psi_n(\vec{r}) = E_n\psi_n(\vec{r}) \tag{1.2}$$

E_n is the eigenenergy corresponding to the state ψ_n. Locally, *i.e.* on a same mirror, the potential term of the Hamiltonian is a function of the single variable z and the wave function can be decoupled in a product of three wave functions, each of one-dimensional space variable. As we are most interested in the expression of the wave function along the z-axis, we simply leave the other two expressions behind; the particle is free along these axes, and the according functions follow a imaginary exponential form $\psi_n(x) = e^{-ik_x.x}$ and $\psi_n(y) = e^{-ik_y.y}$. k_x and k_y are the x and y components of the wave-vector $\vec{k}$. We can consequently write the equation that the one-dimension problem follows in the z-direction:

$$(\frac{-\hbar^2}{2m}\frac{d^2}{dz^2} + mgz + \hat{V}_0\Theta(-z))\,\psi_n(z) = E_n\psi_n(z) \tag{1.3}$$

The mirror gives a very strict boundary condition for $z = 0$. Given that the Fermi potential of the mirror is very large (in the order of 10^{-7} eV) compared to the eigenenergies of the neutrons (merely in the order of 10^{-12} eV [Abele et al.09]), we consider that the wave function is null for z negative; as the wave function is necessarily continuous, we can therefore assume that $\psi(z \leqslant 0) = 0$.

The equation can thus be written:

$$(\frac{-\hbar^2}{2m}\frac{d^2}{dz^2} + mgz)\,\psi_n(z) = E_n\psi(z),\ z \geq 0 \tag{1.4}$$

We introduce the notations $\tilde{z} = z/z_0$, and $z_0 = \sqrt[3]{\frac{\hbar^2}{2m^2g}}$. This gives us a dimensionless equation:

$$(-\frac{d^2}{d\tilde{z}^2} + \tilde{z})\,\psi_n(\tilde{z}) = \frac{E_n}{mgz_0}\psi_n(\tilde{z}) \tag{1.5}$$

For a neutron in the Earth gravitational field, we have $z_0 \approx 5.87\,\mu$m. In our new equation, the factors have whereof no unit. We define z' as the translation of the spoken eigenenergy which has been normalized through the gravitational potential mgz_0, following $z' = \tilde{z} - \frac{E_n}{mgz_0}$:

$$(\frac{d^2}{dz'^2} + z')\,\psi_n(z') = 0 \tag{1.6}$$

This can be identified as the Airy differential equation. Its solution consist of a linear combination of two expressions, one convergent and one divergent when $z \to +\infty$. They are respectively called the Ai and Bi function. Only the first of them is to be considered in our case, since the divergent solution cannot be physically interpreted since the wave function fades for greater values of z. We have a solution of the form:

$$\psi_n(z') = \frac{A}{\pi}\int_0^{+\infty} cos(t^3 + z't)\,dt \tag{1.7}$$

with the offset term possibly equal to any discrete value for which $\psi(0) = 0$, so that the boundary condition given by the mirror can be respected. This function is normalized so that the probability distribution follows the rule:

$$\forall\, m, n \in \mathbb{N}^2, \quad \left| \int_0^{+\infty} \psi_m^*(z)\psi_n(z)\, dz \right|^2 = \delta_{mn} \tag{1.8}$$

Under excitation, a particle can undergo a state transition. In our experiment, the excitation takes place on the two vibrating mirrors, for which the mechanical oscillation can cause a transition for given frequencies. Let us reconsider the differential equation (2.1), with the same assumptions on the particle, except that the potential of the mirror $\hat{V}(z)$ depends now on time, such that its expression becomes:

$$\hat{V}(z,t) = \hat{V}_0 \Theta(-z + a\; sin(\omega t))$$

As the expression reads, the mirror is now under an oscillation at a frequency ω, giving the threshold of the potential a sinusoidal form. The differential equation is modified as follows ([Abele et al.09]):

$$i\hbar \frac{d\psi(z,t)}{dt} = (-\frac{\hbar^2}{2m}\frac{d^2}{dz^2} + mgz + \hat{V}_0\Theta(-z + asin(\omega t))\; \psi(z,t) \tag{1.9}$$

If we use $\hat{z} = z - asin(\omega t)$, we can more easily rewrite our equation, since the boundary condition is no longer $\psi(z = 0) = 0$ but $\psi(z = asin(\omega t)) = 0$:

$$i\hbar \frac{d\hat{\psi}(\hat{z},t)}{dt} = (-\frac{\hbar^2}{2m}\frac{d^2}{d\hat{z}^2} + mg\hat{z} + W(\hat{z},t))\; \hat{\psi}(\hat{z}) \tag{1.10}$$

W is the only time dependent term in our new frame and represents the oscillations of the mirror, as is developed in [Micko18]. To solve this kind of equation, the time-dependent perturbation theory can be used. Details can be found in the mentioned reference. From now on, we leave the notations $\hat{z}$, $\hat{V}$ and $\hat{\psi}$ for z, V and ψ. With the eigenstates of the initial resting wave function, the perturbed wave function $|\psi\rangle = \psi(z,t)$ can be written as their linear superposition:

$$\psi(z,t) = \sum_{k=0}^{+\infty} C_k(t) e^{i\frac{E_k t}{\hbar}} \psi_k(z) \tag{1.11}$$

C_n are vector coefficients functions of time. They express the influence of all bounds states on one another and all have a modulus less than or equal to 1. The work of J. Micko gave us a method to apply equation (10) to these eigenstates, which leads to the following differential equation:

$$\forall\, m,n \in \mathbb{N}^2,\ \dot{C}_m(t) = a\omega cos(\omega t + \phi) \sum_{n=0}^{+\infty} e^{i\omega_{mn}t} V_{mn} C_n^*(t) \tag{1.12}$$

V_{mn} and ω_{mn} are respectively the potential and frequency for a transition from the state n to the higher state m. Their expression reads:

$$\forall\, m,n \in \mathbb{N}^2,\ \omega_{mn} = \frac{E_m - E_n}{\hbar} \forall\, m,n \in \mathbb{N}^2,\ V_{mn} = \int_0^{\infty} \psi_m(z) \frac{d}{dz} \psi_n(z) dz \tag{1.13}$$

We notice that both terms are anti-symmetric in m, n. Some numerical values are shown in the tables below.

m/n	0	1	2	3	4	5
0	0.	97373.5	−53539.9	38301.5	−30393.8	25489.9
1	−97373.5	0.	118935.	−63135.8	44185.7	−34528.6
2	53539.9	−118935.	0.	134572.	−70304.5	48653.3
3	−38301.5	63135.8	−134572.	0.	147213.	−76204.2
4	30393.8	−44185.7	70304.5	−147213.	0.	157984.
5	−25489.9	34528.6	−48653.3	76204.2	−157984.	0.

Figure 1.4: Potentials for the first five eigenstates interaction couples

m/n	0	1	2	3	4	5
0	0.	−254.535	−462.925	−647.101	−815.462	−972.345
1	254.535	0.	−208.39	−392.566	−560.927	−717.81
2	462.925	208.39	0.	−184.176	−352.537	−509.42
3	647.101	392.566	184.176	0.	−168.361	−325.244
4	815.462	560.927	352.537	168.361	0.	−156.883
5	972.345	717.81	509.42	325.244	156.883	0.

Figure 1.5: Transition frequencies between the first five eigenstates

As it is seemingly very complex and does not give an analytical result with an infinite amount of coefficients themselves including an infinite amount of states, it is more convenient to study state transitions regarding only two states. Be $m \in \mathbb{N}$ so that $m \neq n$. This approximation can lead us to a 2×2 matrix expressing the system of differential equations that describes our two-state transition and the amplitude coefficients C_n and C_m.

We get:

$$\begin{pmatrix} \dot{C}_n(t) \\ \dot{C}_m(t) \end{pmatrix} = a\omega cos(\omega t + \phi) \begin{pmatrix} 0 & -V_{mn}e^{-i(\omega_{mn}t)} \\ V_{mn}e^{i(\omega_{mn}t+\phi)} & 0 \end{pmatrix} \begin{pmatrix} C_n(t) \\ C_m(t) \end{pmatrix} \tag{1.14}$$

Although calculations have been made and compared to it, [Killian20] offers the best walk-through towards our result, that we will simply put:

$$\begin{pmatrix} C_n(t) \\ C_m(t) \end{pmatrix} = M(t) \begin{pmatrix} C_n(0) \\ C_m(0) \end{pmatrix} \tag{1.15}$$

This was put for a particle observed initially at $t = 0$. The matrix $M(t)$ is developed:

$$\begin{pmatrix} e^{\frac{i}{2}(\omega-\omega_{mn})t}(cos(\frac{Rt}{2}) - i\, cos(\theta)\, sin(\frac{Rt}{2}) & e^{\frac{i}{2}(\omega-\omega_{mn})t+2\phi}(sin(\frac{Rt}{2})\, sin(\theta)) \\ e^{-\frac{i}{2}(\omega-\omega_{mn})t+2\phi}(-sin(\frac{Rt}{2})\, sin(\theta)) & e^{-\frac{i}{2}(\omega-\omega_{mn})t}(cos(\frac{Rt}{2}) + i\, cos(\theta)\, sin(\frac{Rt}{2}) \end{pmatrix} \tag{1.16}$$

We know ω to be the vibration frequency for the mirror. The new terms R and θ are defined below:

$$a = \frac{2b}{V_{mn}\omega}$$

$$R = \sqrt{4b^2 + (\omega - \omega_{mn})^2}$$

$$b = \frac{R\, sin(\theta)}{2}$$

$$\theta = arccos(\frac{\omega - \omega_{mn}}{R})$$

The solution of $\psi(z', t)\ \forall z', t$ is given in the work from [Micko18]. A transition from a state j to a state k is ruled by the law of probability that we can extract from the scalar product:

$$P(|j\rangle \to |k\rangle) = \left| \int_0^{+\infty} \psi_k^*(z', t)\psi_j(z', t)\, dz' \right|^2 \tag{1.17}$$

For our states n and m,
we define $\Omega = arccos(\frac{a\omega V_{mn}}{2r}$ with $r = \sqrt{(\frac{\omega-\omega_{mn}}{2})^2 + (\frac{a\omega}{2}V_{mn})^2}$.
Some calculation mentioned in appendix A gives us:

$$P(|\psi_j\rangle \to |\psi_k\rangle) = \left| cos(rt) - i\, sin(rt)cos(\Omega) \right|^2 = 1 - sin^2(rt)sin^2(\Omega) \tag{1.18}$$

As could be intuitively foretold, the probability of a transition from a state j to a state k is at its highest at the resonance, *i.e.* when:

$$\omega \rightarrow \omega_{mn} = \frac{E_k - E_j}{\hbar}$$

1.3 Spin polarisation and detection

One of the purposes GRS can serve is to search for what might be gravitational deviations which could be an expression of the Einstein-Cartan gauge theory [Trautman06]. qBounce uses GRS with Ultra-Cold Neutrons for many advantages that must not be overlooked. They are very slow, with a kinetic energy of about 100 neV. This energy is the same order of magnitude as they gravitational potential on Earth at 1 meter height, or as their Zeeman splitting energy under a magnetic field of 1 Tesla. They are also electrically neutral and their polarizability is extremely small, in contrast to atoms, which makes them practically insensitive to any electric field. Finally, neutrons present, additionally to their mass and electric charge, a spin of 1/2. Depending on the orientation of their spin, the neutrons show the influence of a spin-coupling field through their gravitational eigenstates and the corresponding eigen-energies.

Though neutrons bear no charge, they are fermions and thus have a half integer spin, be $S = \pm\, 1/2$. They have an associate magnetic momentum of which formula reads:

$$\mu_n = g_n S \mu_N = \gamma_n \mu_N \tag{1.19}$$

With $\gamma_n \approx -1.8324 \times 10^8\,\mathrm{rad.s^{-1}.T^{-1}}$ the gyromagnetic ratio of the neutrons ([Neutron Booklet03]). This is the ratio between the intensity of a magnetic field and the resulting Larmor precession frequency. This means that a neutron can undergo a modification of the direction of its spin under a magnetic field in specific conditions.

Consider a beam of neutrons travelling horizontally through a polariser set in vertical direction. The kind of spin-polariser for neutrons that we will discuss consists of an iron foil magnetised by a magnet powerful enough to dismiss all neutrons of which magnetic momentum is not in the same direction as the field of the magnet (if they have the same momentum, it means that their spin is opposite to the field). The magnetisation of the foil modifies its Fermi Potential by adding a term of which sign depends on the spin of the particle [Cronenberg16]:

$$V_{F\pm} = V_{F_0} + \vec{\mu_n}.\vec{B} = V_{F_0} \pm \mu_n B \tag{1.20}$$

This equation is simplified for neutrons with vertical spins only. The admittance of the neutrons is possible when their kinetic energy exceeds the Fermi-Potential, which is higher when their spin is in the direction of the magnetic field. Technical specifications about our polariser will be given in 3.1, but for a general idea, the Fermi potential of iron is about 210 neV [Golub et al.91], and the neutron magnetic moment μ_n amounts to $-60,31\,\mathrm{neV.T}^{-1}$ [Beringer et al.12].

If the whole path of the neutrons is also under a vertical magnetic field generated by 2 coils set above and below the installation. The spin momentum of the neutrons will couple with the magnetic field which will keep the spin of the neutrons parallel or anti-parallel to its direction [Cullity & Graham09]. We call this field the guiding field. The principle of the setup is shown in the sketch below:

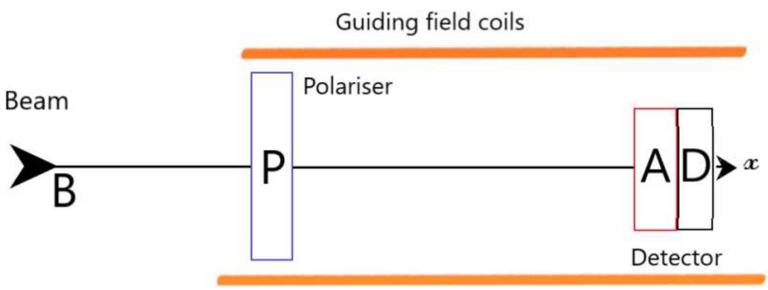

Figure 1.6: Principle of the polarisation-detection setup

The guiding field is arranged in such a way that all neutron spin is oriented either parallel or anti-parallel to the field, following a same axis. The neutrons can then be detected by a neutron detector also consisting of a magnetic field so that only neutrons with a spin in the opposite direction to the field get detected (In the figure, A stands for "Analyzer"). Their coupling between the magnetic momentum the neutrons $\vec{\mu_n}$ and the magnetic field $\vec{B}$ is defined by the following differential equation:

$$\frac{d\vec{\mu_n}}{dt} = \gamma\vec{\mu_n} \times \vec{B} \tag{1.21}$$

All the experimental details concerning the mentioned setup will be spoken in the chapter 3. We will present a theoretical development about polarisation and spin-flipping in the next chapter.

Chapter 2

Polarisation and spin-flip theory

Neutron polarisation is the essential feature of our experiment and its potential value for the qBounce experiment, as discussed in the previous chapter. For our measurements to be relevant, we need to establish the relations binding the properties of our components and the results we obtain.

What we will look for in this chapter is to fully understand how neutrons behave under certain magnetic conditions, how one can determine and control their polarisation, and what one can exploit from it. We will first break through a theoretical description of the beam-polarisation in our kind of experiment; we will then present the notion of spin-flip and its use in polarisation measurements.

2.1 Relations between the expected detection rates and the polarisation efficiency

We already stated in 1.3 that the magnetisation of the iron foil of the polarizer drove to a modification of its Fermi-potential with a dependence on the spin-direction of incoming neutrons (see equation 1.20). For a given velocity, the polarisation efficiency, *i.e.* the ratio of neutrons with the right spin-direction over all incoming neutrons, does not depend on the intensity of the magnetic field. However, in order for the polarizer to work on faster neutrons, the Fermi potential has to exceed the potential of neutrons with the wrong spin with the help of its field-dependent component. By the same token, the Fermi potential for neutrons with the right spin-direction is also spin-dependent and can be lowered so that slower neutrons with the right spin can add-up to the beam. In other words, the stronger the field B driven through the magnet is, the wider is the neutron-energy window within which the polarisation can be effective.

In respect to the schematic description of the installation that we offered in the previous chapter, the spin of the neutrons aligns to the gravitational field; in our setup, the coils are not horizontal, but are set in such a way that the value of the magnetic field presents a gradient along the beam. A schematic representation is displayed in the next chapter (see 3.1).

Nevertheless, its direction is still vertical because the angles between the coils and the horizontal are identical, and the non-vertical terms of the resulting magnetic field cancel out.

We will refer to the spin of the neutrons as *down*, for when the spin points to the ground, and *up* when it points to the sky. Their detection rate is spin-dependent because the detector at the end of the beam acts as an analyser, which is how we will refer to it when studying the polarising properties of the detector.

The polarisation rate of a polariser, which defines its efficiency, is written for the general case:

$$P_\uparrow = \frac{N_\uparrow - N_\downarrow}{N_\uparrow + N_\downarrow} = -P_\downarrow \tag{2.1}$$

Let P_p and P_a be respectively the polarisation rates of the polariser and the analyser. They follow the equation:

$$P_{p\uparrow} P_{a\uparrow} = \frac{N_\uparrow - N_\downarrow}{N_\uparrow + N_\downarrow} \tag{2.2}$$

A result for the case of identical polarizers is explained in the work of [Cronenberg16]. In our case, this result cannot be exploited and we must use the general equation to find out the rate of the polariser.

The analyser is polarised using a magnetic field that can be adjusted; we can set the intensity manually, invert the poles or turn it off. We can find a useful notation formalism in [Soldner] consisting of matrices. With a restriction to the special case of neutrons of which kinetic energy exceeds the Fermi potential of the iron foil (210 neV), we can write the transformations of the beam by the components as a product of corresponding matrices:

$$\mathbf{D}\mathbf{A}_1\mathbf{P}_1\mathbf{B} = \begin{pmatrix} d & d \end{pmatrix} \begin{pmatrix} 1 & 0 \\ 0 & 1-A_1 \end{pmatrix} \begin{pmatrix} 1 & 0 \\ 0 & 1-P_1 \end{pmatrix} \begin{pmatrix} n/2 \\ n/2 \end{pmatrix} \tag{2.3}$$

D, $\mathbf{A}_1$, $\mathbf{P}_1$ and **B** stand respectively for the detector, the analyser when the field is in the direction of the polariser, the polariser and the beam. The factors P_1 and A_1 are related to the polarisation rates P_p and P_a for the chosen setup, so that $P_p = \frac{P_1}{2-P_1}$ and $P_a = \frac{A_1}{2-A_1}$. In our description, both the analyser and the polariser are set in the same direction. Given that n is the number of neutrons emitted in the beam, the result of this matrix product is directly given by the count of neutrons n_{up} measured by the detector. The factor d is a constant corresponding to the detection rate of the detector. The equation yields:

$$n_{up} = d\left(1 + \frac{P_1A_1 - P_1 - A_1}{2}\right)n$$

With a similar measurement, but with the analyser set in the opposite direction, the matrix product gives:

$$n_{down} = \mathbf{DA}_2\mathbf{P}_1\mathbf{B} = \begin{pmatrix} d & d \end{pmatrix} \begin{pmatrix} 1 - A_2 & 0 \\ 0 & 1 \end{pmatrix} \begin{pmatrix} 1 & 0 \\ 0 & 1 - P_1 \end{pmatrix} \begin{pmatrix} n/2 \\ n/2 \end{pmatrix} \tag{2.4}$$

This yields:

$$n_{down} = d\left(1 - \frac{P_1 + A_2}{2}\right)n$$

The physical interpretation of these matrices is that the polariser (and the analyser) reflects neutrons with the wrong polarisation with an efficiency P_1 (A_1, A_2), and lets through all neutrons with the right polarisation. We can theoretically calculate d with a measurement made when the polariser is not set and the analyser is off. However, we need not calculate this rate for the factors that interest us to find out the polarisation rates. A measurement n_{off} made without the coils of the detector helps us calculate the efficiency of the analyser with the following equation:

$$n_{off} = \mathbf{DP}_1\mathbf{B} = \begin{pmatrix} d & d \end{pmatrix} \begin{pmatrix} 1 & 0 \\ 0 & 1 - P_1 \end{pmatrix} \begin{pmatrix} n/2 \\ n/2 \end{pmatrix} = nd\left(1 - \frac{P_1}{2}\right) \tag{2.5}$$

With the help of a measurement n_{alu} made when the polariser is off (see in the next chapter), we can deduce a relation between P_1 and A_1 from the following:

$$n_{alu} = \mathbf{DA}_1\mathbf{B} = \begin{pmatrix} d & d \end{pmatrix} \begin{pmatrix} 1 & 0 \\ 0 & 1 - A_1 \end{pmatrix} \begin{pmatrix} n/2 \\ n/2 \end{pmatrix} = nd\left(1 - \frac{A_1}{2}\right) \tag{2.6}$$

The relation reads:

$$\frac{n_{off}}{n_{alu}} = \frac{2 - P_1}{2 - A_1} \tag{2.7}$$

2.2 Spin-flip and Larmor frequency

The key phenomenon that we make use of for our experiments is the effect of an oscillating magnetic field on the spin of the particles. A spin-flipper consists of a coil of which axis of the spires is parallel to the beam of particles. The coil receives alternative current, allowing the field that it generates to oscillate over time. Its frequency must be set to coincide with the Larmor frequency of the neutrons in the guiding field at the location of the coil. The Larmor frequency is the precession frequency of the neutrons under a magnetic field, and follows the relation of proportionality:

$$f_L = \frac{\omega_L}{2\pi} = -\frac{\gamma_n B}{2\pi} \tag{2.8}$$

γ_n is the gyromagnetic ratio of the neutron; additionally to the definition given in the previous section, the gyromagnetic ratio is proportional to the magnetic moment of the neutron: $\gamma_n = \frac{\mu_n}{\hbar}$. To allow the spin-flip to occur, we have to set the guiding field with a gradient following the x-axis.

A neutron travelling through a spin flipper will be subject to the guiding field $\vec{B_0}$, which is oriented in the z-direction, and the oscillating field of the spin flipper $\vec{B_1}$ along the direction of the beam, that we will name the x-axis, and of which origin will be the middle of the spin-flipper. The magnetic field as a function of space and time reads:

$$\vec{B}(\vec{r}, t) = \vec{B_0}(\vec{r}, t) + \vec{B_1}(\vec{r}, t) \tag{2.9}$$

$B_0 = B(0)$ does not depend on time but only on space such that $B_0(x) \approx -\alpha B(0)(x - x_0)$ where α is the gradient factor (expressed in m^{-1}) that depends on our installation and that we measure in the next chapter, and x_0 is the extrapolated null-point of the field that can be found with the gradient factor α. We will find out in the next chapter that this point is far enough away from our study point for the approximation to be valid. $\vec{B_1}$ is a homogeneous oscillating field rotating normal to the z-axis with given frequency Ω and intensity B_1 such that $\vec{B_1}(t) = B_1\, cos(\Omega t)\vec{u_x} + B_1\, sin(\Omega t)\vec{u_y}$. We have to consider the equation (30) locally, where the oscillating field is maximal. We can write it:

$$\vec{B}(\vec{r}, t) = B_0(x)\vec{u_z} + B_1\, cos(\Omega t)\vec{u_x} + B_1\, sin(\Omega t)\vec{u_y} \tag{2.10}$$

With a transformation from the rest frame to the rotating frame of the neutron, the expression of the magnetic field as seen by the neutron are changed. It yields:

$$\vec{B}(\vec{r},t) = (B_0 - \frac{\Omega}{\gamma_n})\vec{u_z} + B_1 cos[(\Omega - \omega_L)t]\vec{u_x} + B_1 sin[(\Omega - \omega_L)t]\vec{u_y} \quad (2.11)$$

It is particularly relevant at the resonance, $i.e.$ where $\omega_L = \Omega$. Since the Larmor frequency is given by the magnetic field B_0 normal to the direction of the spin, $B_0 = \frac{\Omega}{\gamma_n}$ and the terms cancel out. At the resonance, the expression of the magnetic field is reduced to:

$$\vec{B}(\vec{r},t) = B_1\vec{u_x} \quad (2.12)$$

It means that the neutrons are not under a vertical magnetic field anymore at the place where the resonance occurs. The perturbation given by the oscillatory field on their spin can cause a spin-modification. However, it needs not only these conditions to be fulfilled in order for the spin-flipping process to occur optimally. We need to create the conditions for an adiabatic spin-flip. Physically, a spin flip is considered adiabatic if the vertical magnetic field in the rest frame is very large in comparison to the time derivative of the magnetic field in the rotating frame of the particle. It can be found in [Seo et Al.07], that the probability of a spin depends exponentially on this ratio. With a factor ω_L, we define the adiabatic parameter:

$$\lambda = \omega_L \frac{B_0}{\dot{B}_0}$$

This parameter must be as large as possible for the probability of a spin-flip to be maximal. For a neutron with a speed v_n in the x-direction, the term $\dot{B}_0$ can be linked to the space derivative $\frac{dB_0}{dx}$. The adiabatic condition is thus:

$$\omega_L B_0 >> v_n \left| \frac{dB_0}{dx} \right| \quad (2.13)$$

When this condition is met, the probability of a spin-flip when a neutron encounters the resonance is approximately 1 [Taran75]. The inequality can be rewritten with the factor α and interpreted numerically, for the fastest neutrons in our interest ($v_n = 25\,\mathrm{m.s^{-1}}$):

$$\frac{\alpha B_0}{B_0^2} = \frac{\alpha}{B_0} << \frac{\gamma_n}{v_n} \approx 7.10^7\, m^{-1}T^{-1} \quad (2.14)$$

It means that the condition is easier to meet, the greater the guiding field is.

The graphic shows that, for a field down to 0.5 mT, a field gradient of $\approx 2\,\mathrm{mT.m^{-1}}$ yields us $\lambda \approx 10$, which makes it already acceptable for the

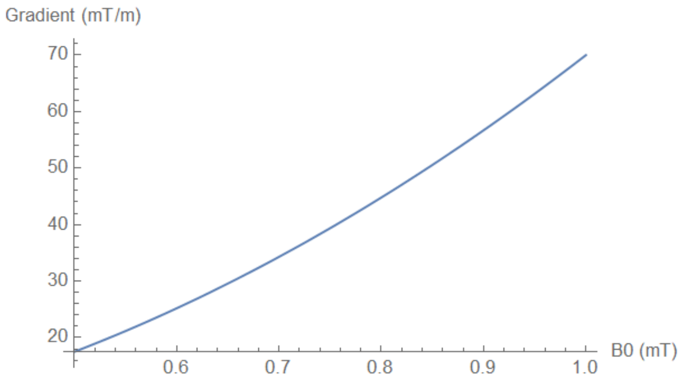

Figure 2.1: Field gradient in relation to the field for $\lambda = 1$

approximation of the adiabatic spin-flip. We will see in the next chapter that it is rather easy to meet this condition with our experimental setup.

Following the model that we presented in the section 2.1, to a spin-flipper with an efficiency F will correspond the following matrix **F**:

$$\mathbf{F} = \begin{pmatrix} 1-F & F \\ F & 1-F \end{pmatrix}$$

The beam will then be transformed accordingly:

$$\mathbf{DA_1FPB} = \begin{pmatrix} d & d \end{pmatrix} \begin{pmatrix} 1 & 0 \\ 0 & 1-A_1 \end{pmatrix} \begin{pmatrix} 1-F & F \\ F & 1-F \end{pmatrix} \begin{pmatrix} 1 & 0 \\ 0 & 1-P \end{pmatrix} \begin{pmatrix} n/2 \\ n/2 \end{pmatrix} \tag{2.15}$$

In this situation, the analyser and the polariser are in the same direction. The neutron rate n_{flip} is consequently calculated:

$$n_{flip} = dn\left(1 + \frac{A_1 - P + A_1 P - A_1 F P}{2}\right) \tag{2.16}$$

We get F in function of A and P in the appendix, along with some plots showing F for different values of A and P.

Chapter 3

The Test-Beam experiment

The experiment that we lead was bound to help us know the properties of our experimental instruments. Using the Test Beam, we wanted to learn about the polariser, the spin-flipper and the detector with the help of several measurements. These measurements are discussed at the end of the chapter, while the needs of the experiment that we carried out is developed beforehand, along with the experimental apparatus itself, in the next 2 sections.

3.1 Working principle

The qBounce experiment is now to look for possible spin-dependent deviations [Cronenberg16] and to search for a particle mediating this spin-dependent form [Jenke11]; as already mentioned, we need to create a polarised beam of neutrons, hence the use of a polariser and an analyser, and to study the effects of a spin-flip on the neutrons with a spin-flipper.

3.1.1 Needs of the experiment

Our experiment involves a unidirectional, depolarised beam of UCN that we will put under polarisation and analysis. We need to create a vacuum in order for the beam to reach the detector with a high enough rate. For the core of the experiment, as discussed, we need the polariser, a spin-flipper of which intrinsic properties are known or measured beforehand, and the detector, that can be polarized with coils. We also need large coils to generate a guiding magnetic field over all the experimental setup, as stated in the previous section.

The beam had to be guided through a set of pipes that would link all the devices of the experiment. They had to be hermetically fixated to the instruments to allow a vacuum. The power supply used for the coils needed to be powerful enough to create a magnetic field that would dominate any perturbing field. The power supply also had to provide an alternative current in the radio-frequency realm ($\approx 20\,\mathrm{kHz}$) with the help of an amplifier. Details concerning this choice of frequency will be given in the section 3.2. We had to check that the coils would not create any fire hazard due to the Joule-effect under high intensity current, and to set them in order to comply with safety. A compromise had to be found, because we wanted the guiding field to be as strong as possible for precision purposes (see 3.2).

The neutrons having disparate velocities (mainly from $5\,\mathrm{m/s}$ to $15\,\mathrm{m/s}$), the efficiency of the instruments on them is various. Faster neutrons, for instance, are less likely to be reflected by the polariser even though they are in the wrong polarisation. They "see" a steeper magnetic gradient, making the adiabatic condition more difficult to meet and the spin-flip consequently less likely to occur. If we measured the incoming neutrons as a continuous flux, the amount of information that we could get with the measurements would be very limited, as the different velocities would be indistinguishable. This is where a chopper comes in useful. It is in principle a shutter opening and closing for given times so that the neutrons come by bursts. Its functioning is further explained in 3.2.2. With a chopper, the signal that we can get is no longer a flat line, but periodic peaks coming a short time after the aperture of the chopper. The amount of time corresponds obviously to the travelling time of the neutrons, the so-called time of flight (or tof). Thanks to this feature, the signal can be sorted according to velocity and speed-dependent effects can be put in light.

The general sketch of the experiment is shown below:

In this sketch, the vacuum pumps, the power supply and the amplifier are not shown.

For the calculations concerning the velocity of the neutrons, we measured the distance between the chopper and the detector to be $1.06\,\mathrm{m}$, that we labelled "Distance of Flight".

3.1.2 Protocol for different measurements

We prepared a protocol to determine what measurements would serve our goals, which are to find out the efficiency rates of the detector, the polariser and the spin-flipper. Ground measurements were first necessary, in order to check that neutrons could go through the beam and could be detected at all. For ground measurements, the coils are all turned off, and so is the chopper. It means that the analyser function of the detector, the spin-flipper and the guiding fields are ineffective. The detected signal could be sorted by

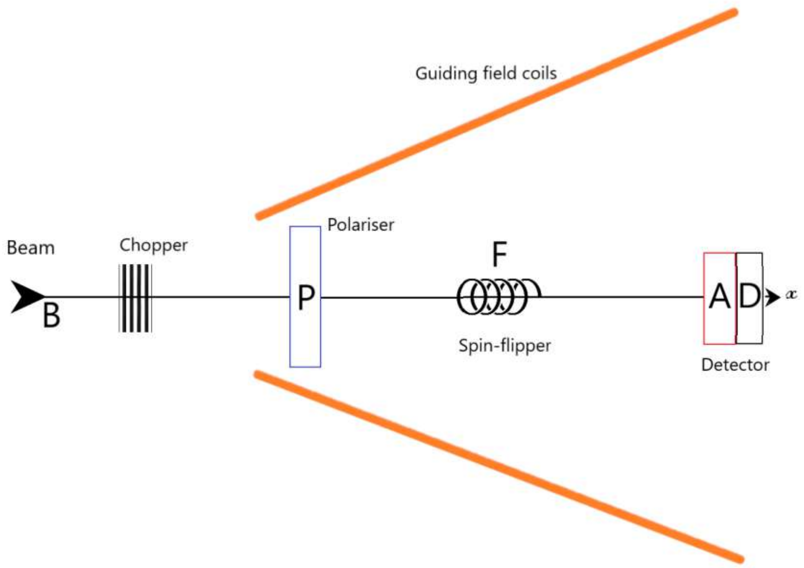

Figure 3.1: Side view of the schematic setup

frequencies and an energy spectrum could let us see different peaks that are explained in 3.2.2.

The chopper was then turned on in order to build a ground velocity spectrum with the measured data. The guiding field was then turned on for the rest of the measurements. We planned eight different measurements for each arrangement of the detector (field *up* or *down*), the polariser (with the iron foil and the aluminium foil, see 3.2.1) and with or without the spin-flipper.

3.2 Description of the setup

The Test-Beam, on which we carried out our experiment, is a low-flux beam of which name is quite explicit as it is dedicated to test experiments such as our own. We worked during the 189th reactor cycle of the ILL, which took place from January the 28th to March, the 30th 2021. It included at first a thorough study of the instruments that we were handed, because we had to ensure ourselves that they were fit for our requirements.

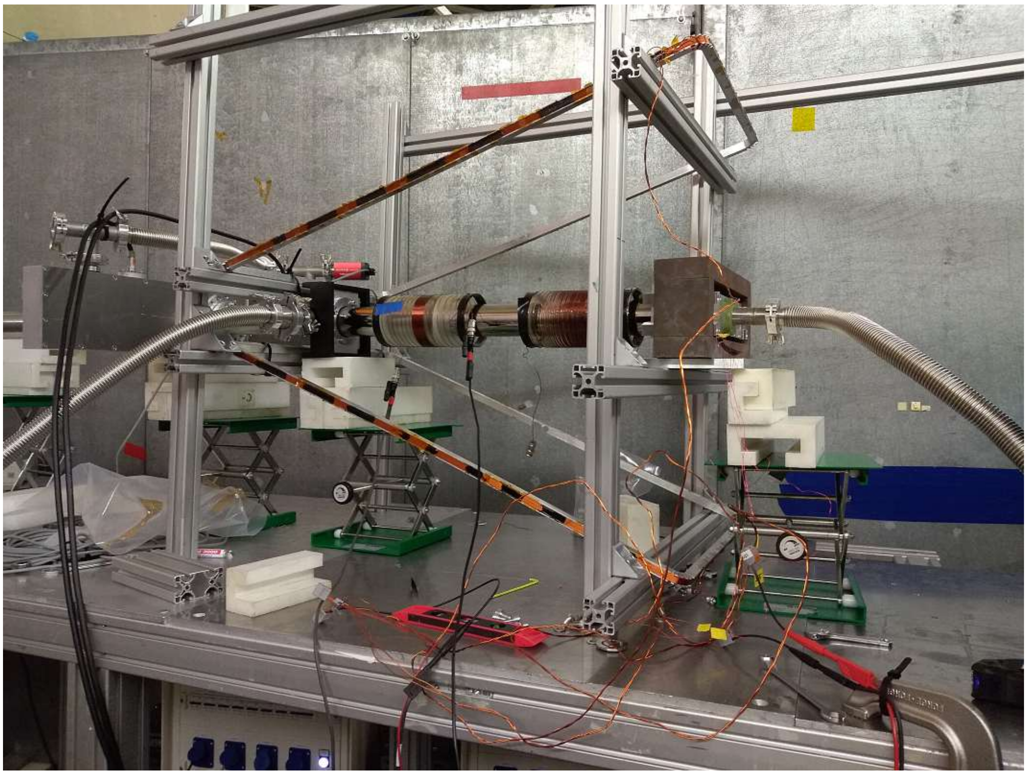

Figure 3.2: Picture of the Test-Beam Experiment. We can see the polariser surrounded by black plates, where the pipe of the vacuum pump takes the air from, then the beam going on the right, through the first and the second spin-flipper, and finally the detector, within the massive metallic frame.

3.2.1 Characterisation of the detector

The detector is equipped with a Boron layer (80.1% ^{11}B, 19.9% ^{10}B) which reacts with incoming neutrons according to the following nuclear reaction:

$$\begin{aligned} {}^{10}B + n &\longrightarrow {}^{7}Li^{*} + \alpha + 2.79\,MeV \\ &\longrightarrow {}^{7}Li + \alpha + \gamma(0.48\,MeV) + 2.31\,MeV\ (94\%) \end{aligned} \tag{3.1}$$

$$ {}^{10}B + n \longrightarrow {}^{7}Li + \alpha + 2.79\,MeV\ (6\%)$$

The detection of the scattered ions is done by a proportional counter tube, which is an anode wire within an airtight cylinder filled with $ArCO_2$. Argon is the gas to be ionised by the fission products, while carbon dioxide is a quenching gas [Rechberger18]. The electrode will measure the charge provoked by the ionisation of Argon. Depending on the energy of the detected ion, the detector allows us to distinguish the detected product.

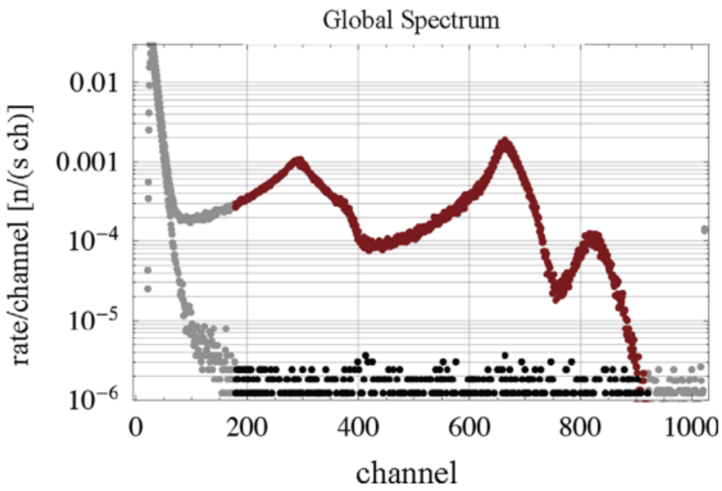

Fig. 10. Total energy spectrum and background behaviour of our UCN counter. All measurements performed in our beam time in 2012 are summed up and divided by the total measuring times. The optimal ROI [180, 920] regarding signal-to-noise is indicated in red (black). The exponential increase toward smaller channels originates from electronic noise. A hardware threshold rejects signals with very small pulse heights (adapted from: [26, Fig. 4.9, p. 55]). (For interpretation of the references to color in this figure legend, the reader is referred to the web version of this article.)

Figure 3.3: Spectrum as shown in [Jenke et al.13]

It is best explained in [Jenke11] that each incoming neutron yields exactly one fission product for detection: because of momentum conservation, and because the kinetic energy of incoming UCN is negligible compared to the energy of the fission, only one of the two products will continue towards the counter tube. The thickness d of the boron is key for an optimal detection: too thin, and only a small amount of neutrons will react with the boron; too thick, and most of them will not be able to reach the counter tube. Further details can be found in [Saul11].

The boxing of the detector is made of brass plates of screwed together, forming a parallelepiped of dimensions 236.2 mm×82.2 mm×61.2 mm. The entrance plate has a slit of dimensions 89.0 mm×6.0 mm and holds an iron foil that can be polarised by the two coils set on top and bottom of the detector. The work [Cronenberg16] indicates us that the required magnetic field in order to polarise the foil sits between 5.4 and 5.7 mT, and it takes a field of 1.1 mT to maintain this polarisation and protect it from underground magnetic perturbations. The magnetic profile around the detector was drawn for several values of the voltage set for the coils.

The whole was firmly held in a large iron frame which prevented any accidental displacement of the detector during or between the measurements.

In a test setup, we measured the overall rates with different values of field going through the detector foil, with the spin-flipper turned on. The goal was to test the efficiency of the spin-flip qualitatively. We assumed that if the foil was polarised opposite to the magnetic field of the polariser, we would obtain opposite results, *e.g.* a higher rate with the spin-flipper than without it. However, the results differed. The measurements were made with voltages going from -4 V to $+4$ V, and we drove a -16 V (resp. $+16$ V) voltage through the coil when we reached -4 V (resp. $+4$ V). The foil has a magnetisation memory, meaning that we expected the polarisation to be more efficient after the voltage peak.

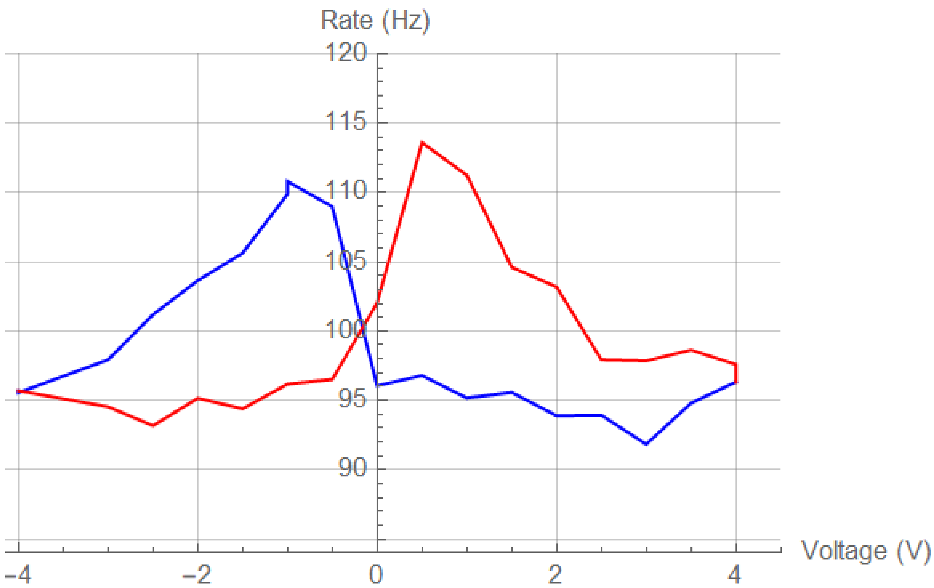

Figure 3.4: Rates measured for different values of voltage for the detector foil. In red, the measurements were made with ascending voltages and in blue with descending voltages. The dashed curves represent what we qualitatively expected from the theory.

With the magnetisation memory of the foil, we expected the curves to be distinct by an offset, which proved right on the experiment and for positive values of voltage. The $+16$ V peak is slightly noticeable.

For negative values, however, the measured data differ much from the expectations. The experiment shows a symmetry between upwards and downwards polarisation of the detector foil, as if the polarisation were in the same direction.

The magnetic profile near the detector pictured in 3.9 can help understand this phenomenon: the continuity of the magnetic field along the beam and its opposite signs at the detector and the polariser causes a zero-point to appear. There must be a place along the neutron path at which the vertical component of the magnetic field is 0. This means that the adiabatic condition of the spin-flip is no longer met, and the polarisation of the neutrons can be other than predicted. The experiment shown in 3.4 gives some indication in this direction.

3.2.2 Description of the whole installation

The Test-Beam provided us with a steady source of neutrons that we drove in a straight line through our device. We installed tubes of which inside was made of glass to prevent air leaks. They were connected to the instruments with airtight joints. We used a set of two vacuum pumps: one of them is a turbo-molecular pump, working very efficiently to create a rough vacuum from atmospheric pressure, and another one more sensitive and which can only work with a pre-vacuum and enhances it to a fine vacuum. Many hermeticity tests have been lead to ensure a good vacuum in the experimental device. Our best results went to 2.10^{-3} mbar in the chamber.

The neutrons travelling through the glass tube were sorted by a chopper made of opaque vertical blades shutting on each other. The aperture of the shutters has been programmed to open for 20 ms every 800 ms. Its aperture in function of time is shown on the table below.

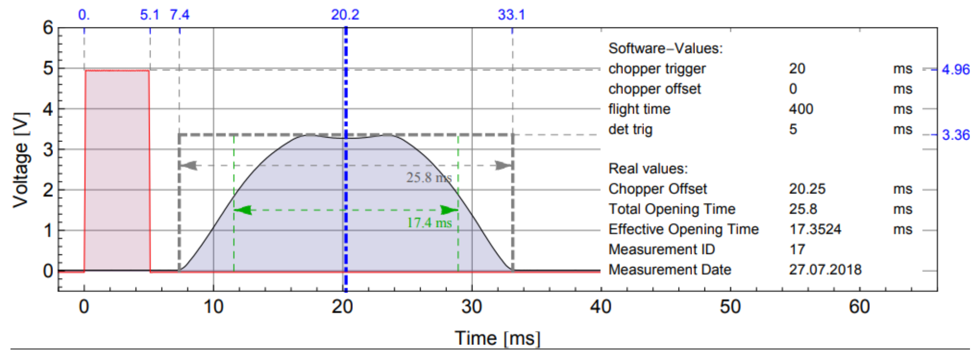

Figure 3.5: Aperture of the chopper after the opening signal

The polariser consists of an iron foil held in an iron frame on which magnets all around sticked in order to concentrate the magnetic lines around the polariser. Its magnetic profile is shown on the drawing below.

We were unable to measure the magnetic profile in the nearest proximity of the foil, due to the size of the probe, hindering us from having a reliable

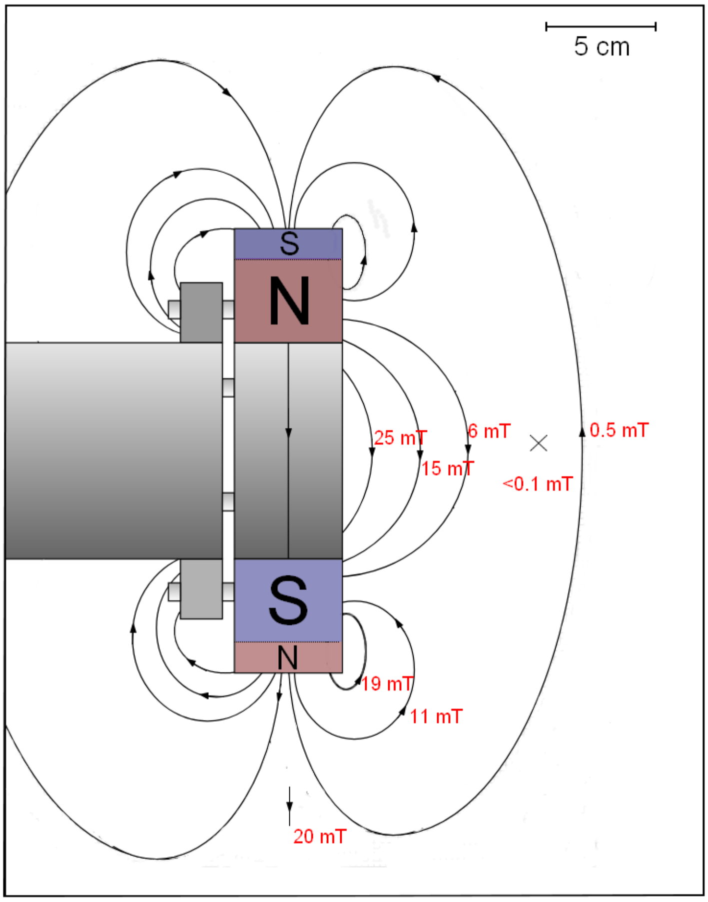

Figure 3.6: Magnetic profile of the polariser. Neutrons go through the beam from the left to the right. The foil is represented by the vertical line between the magnets.

measure in the small space around the polariser. The magnetic range of our device restrained us to a careful measurements, and we avoided to measure above 100 mT, at about 3 cm from the foil.

It is possible to remove the iron foil. We also had an aluminium foil of the same dimensions that could be put instead. Since aluminium is insensitive to magnetic fields under atmospheric conditions ($T \approx 295.6\,\mathrm{K}$,$P \approx 1\,\mathrm{atm}$), the foil is not magnetic and the beam of neutrons that goes through it stays depolarised. Its Fermi potential is worth approximately 54 neV, which is below the Fermi potential of iron. Any neutron with enough kinetic energy to go through iron has enough to go through aluminium. The presence of a foil reduces the background signal by stopping the slowest of neutrons that come in the beam. Due to the nature of the measurement, the neutrons that interest us have a kinetic energy just above the Fermi-level of iron, as these can only be stopped by the polarisation of the foil. This realm, that we call *Region of Interest* (*ROI*), is the energy region above 210 neV. We remind that the polarisation allows a window of 60.31 neV.T^{-1}. Despite our inability to measure the magnetic field right in the iron foil, we know for a fact that it cannot exceed a few *Teslas*, given its nature: the magnetic field is created by permanent magnets. It means that our *ROI* is capped at highest by an energy of 450 neV (for a magnetisation of 4 T), which corresponds to a neutron velocity of 9.3 m.s^{-1}.

Two large rectangular copper coils were installed above and under the beam. The coils were very close to identical, both having the same dimensions (90 cm×50 cm×1.5 cm) and the same resistance (≈ 1.5 Ω at 23°C). After theoretical calculus, it was stated that they could bear a current up to 8 A and stay below 60°C. A test proved right with a stabilised temperature around 35°C for a current of 5 A. This amount of current has been used for the entirety of the experiment. An angle was created between them to yield a field gradient along the direction of the beam. The magnetic field in the z-direction was thoroughly measured around the setup with a probe sensitive down to 10^{-6} T.

The magnetic field needed to be strong enough for the reasons mentioned in 3.1.1. We measured the profile of the magnetic field for a current of 2 A.

We were provided with two different spin-flippers for the purposes of the experiment. They both lie on the very same principle: a copper coil of which winding is tighter in the center and looser at the ends of the coil. The support of the coil is a cylinder of length 20 cm and of diameter 10 cm. The cylinder is made of plastic to minimize its influence on the magnetic field. Their picture along with a graph showing their magnetic profile are are shown below.

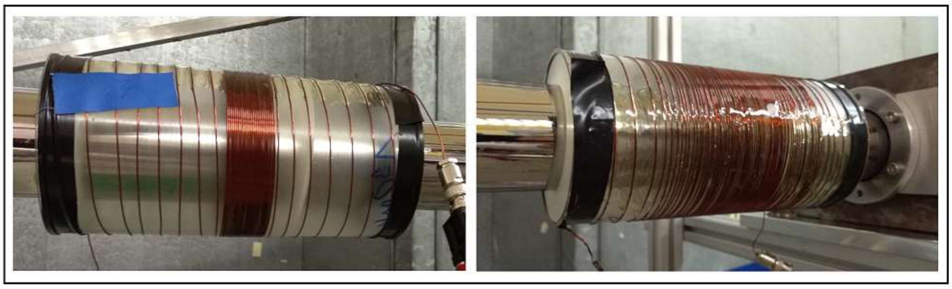

Figure 3.7: Magnetic profile longitudinal to the coils, from the left to the right.

For our experiment, the first one of them has been exclusively used.

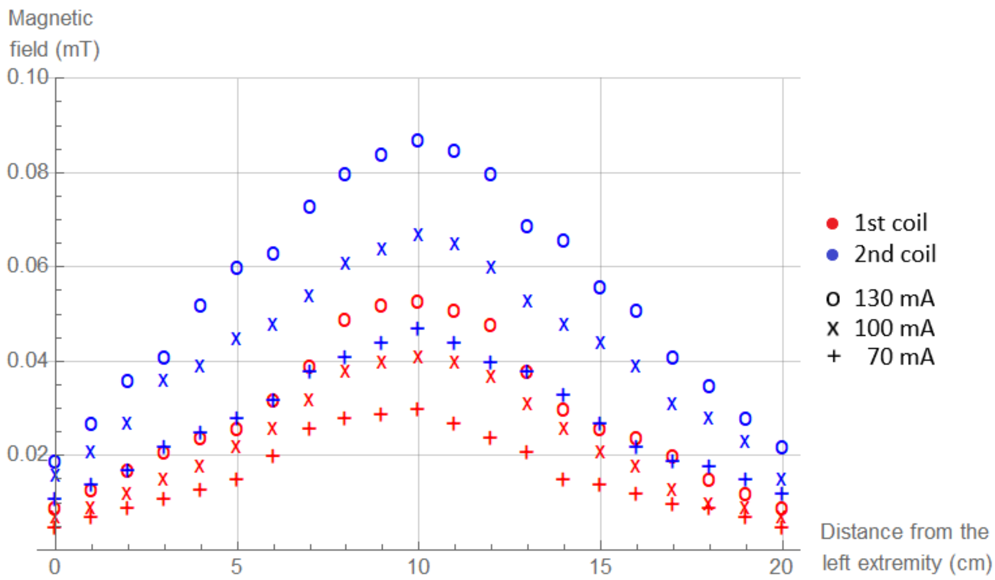

Figure 3.8: Magnetic profile longitudinal to the coils, from the left to the right.

All coils were given current by a power supply able to deliver either direct or alternative current at a voltage up to 100 V. The frequency range of the alternative current is up to 50 kHz. The guiding field coils were given a voltage of 7.5 V, the resulting current was initially 5.05 A but dropped to 4.975 A due to the warming of the coil, giving it a higher resistance. the spin-flipper was delivered various voltages for various frequencies, which will be further discussed in 4.3.

The whole magnetic profile of the installation is given for 5 A in the following sketch:

Thanks to this profile, we determine the necessary frequency of the spin-flipper to match the Larmor-frequency locally corresponding to the guiding field:

$$\omega \approx \Omega_{Larmor} = \gamma_n B \tag{3.2}$$

If we admit that the magnetic field is proportional to the intensity of the current given to the coils, it means that the wanted frequency is also proportional to the intensity, such that:

$$\omega = \gamma_n \sigma I \tag{3.3}$$

In our case, $\sigma \approx 0.104\,\mathrm{mT.A^{-1}}$. We thus consider that the target frequency depending on the intensity is approximately $3\,\mathrm{kHz.A^{-1}}$.

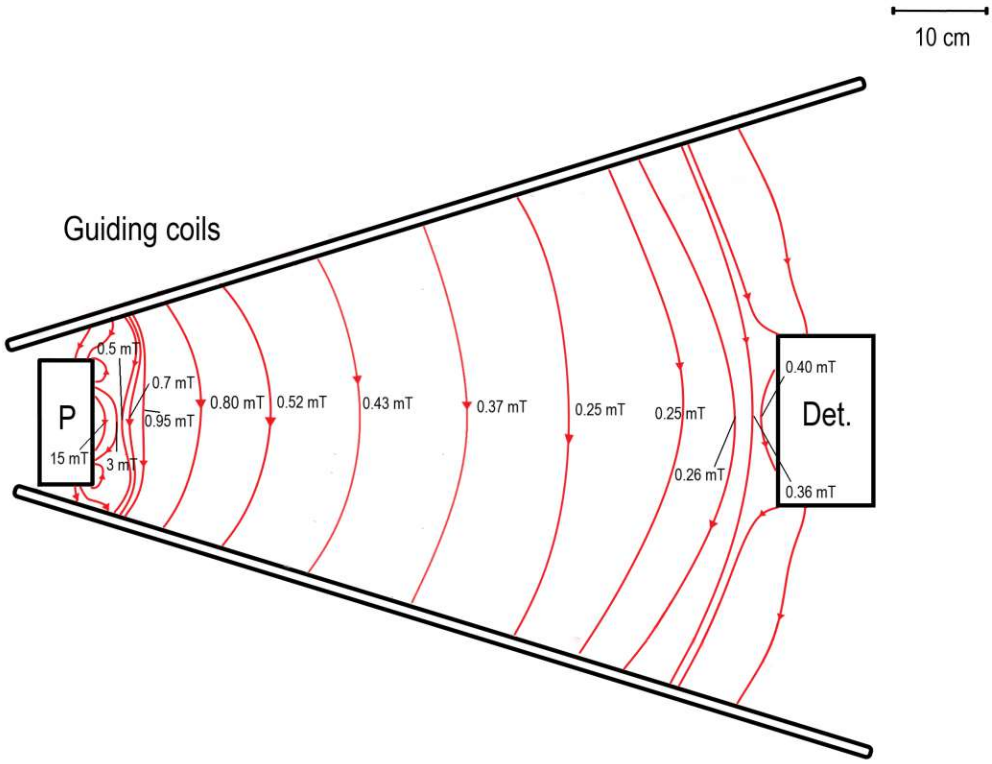

Figure 3.9: Magnetic profile of the whole installation; the detector has a built-in polariser. Most of the values were likely underestimated because they could not be taken at the exact center (the guiding tubes and the spin-flippers were already installed).

The magnetic field must also allow the adiabatic condition given in 2.2 (equation 2.20) to be respected, that we can now link to the intensity. Consequently, the intensity must follow the condition:

$$\begin{aligned} \frac{\alpha}{\sigma\, I} &<< \frac{\gamma_n}{v_n} \\ I &>> \frac{\alpha\, v_n}{\sigma\, \gamma_n} \end{aligned} \tag{3.4}$$

We determine $\alpha \approx 4\,\mathrm{m}^{-1}$ with 3.9. For the fastest neutrons ($25\,\mathrm{m.s}^{-1}$)), we calculate:

$$\frac{\alpha\, v_n}{\sigma\, \gamma_n} \approx 33\, mA \tag{3.5}$$

The condition is thus perfectly met with an intensity of 5 A, intensity for which it is established that the fire hazard is negligible. This is especially true for our *ROI* (mentioned in 2.1), which encompasses neutrons of velocity between 3 and, give or take, 9 m.s^{-1}.

For such an intensity, we should expect the optimal spin-flipper frequency to neighbour 15 MHz.

If the detector is magnetized in the other direction, the magnetic profile shown in 3.9 changes in the vicinity of the detector, as shown below.

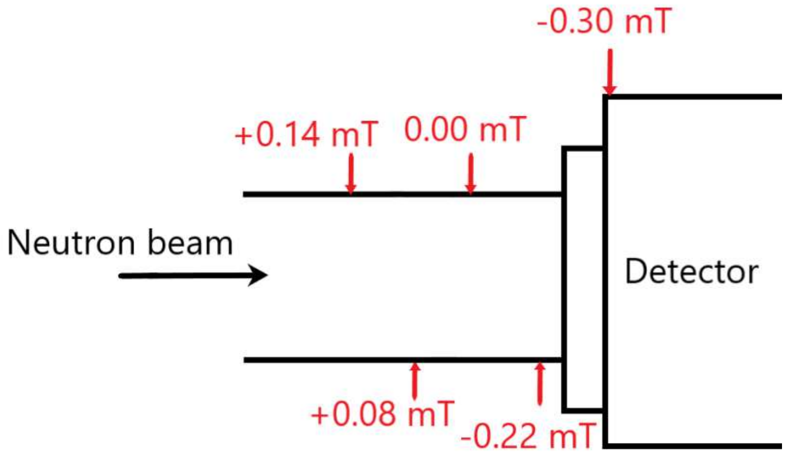

Figure 3.10: Magnetic profile near the detector polarised in the *up* direction.

Chapter 4

Data analysis and interpretation

During the cycle n°189 of the reactor, which took place at the ILL at the beginning of 2021, we could carry out different measurements that could prove useful for the characterisation of our instruments.

After the complete installation of the core instruments and of the computer that received the measured data, we began our measurements with test measurements. The test measurements helped us anticipate the rate we should expect and thus the time needed for each measurement to get consistent data.

4.1 Data treatment and computation

Overall, 18 measurements have been recorded, including 7 that lasted between 10 and 24 hours and which were exploitable for our analysis.

The first test measurement, done without the chopper or any magnetic field, lasted 100 s and yielded a rate of 131 ± 1 Hz. Then we used the chopper to sort the neutrons by velocity. With an aperture time of roughly 20 ms every 800 ms, we expected the rate to be between 2 and 4 Hz, which proved true on the first test measurement with the chopper. This measurement gave a rate of 2.795 ± 0.012 Hz over roughly 40 mn. The data was grouped by bins of 1 ms, from 0 to 780 ms following the aperture of the chopper.

We extrapolated the rates we would obtain for the bins with the least counts within the velocities that we consider, meaning going from 3 m.s^{-1} to 15 m.s^{-1}. The error to be considered in the bin counts follows a Poisson Law.

The fastest neutrons bin includes neutrons from 14.75 to 15 m.s^{-1}, which corresponds to 70.67 to 71.86 ms. It means that each velocity bin will be allowed at least 1 ms worth of counts.

The first ground measurement lasted 66031 ± 0.2 s and was also made without any magnetic field turned on.

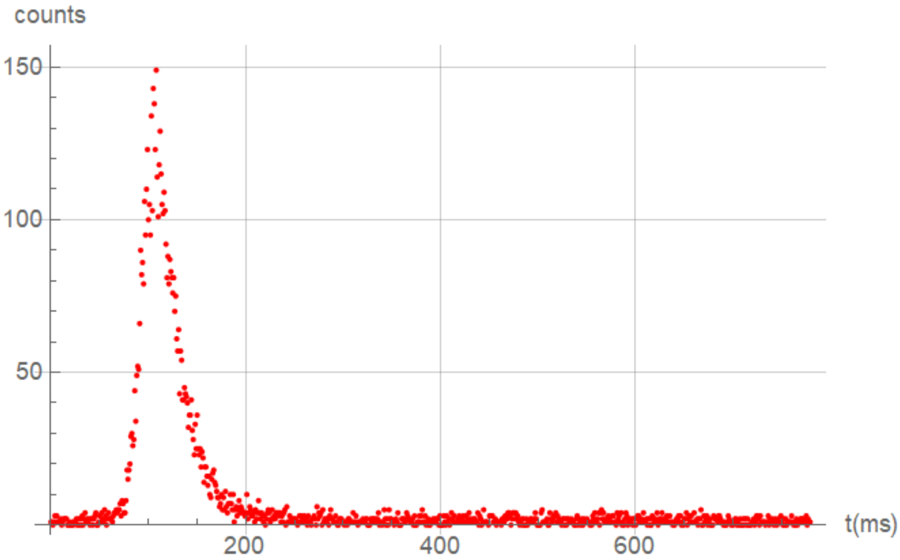

Figure 4.1: Test measurement with all fields turned off and the chopper on, for a time of 2433 s.

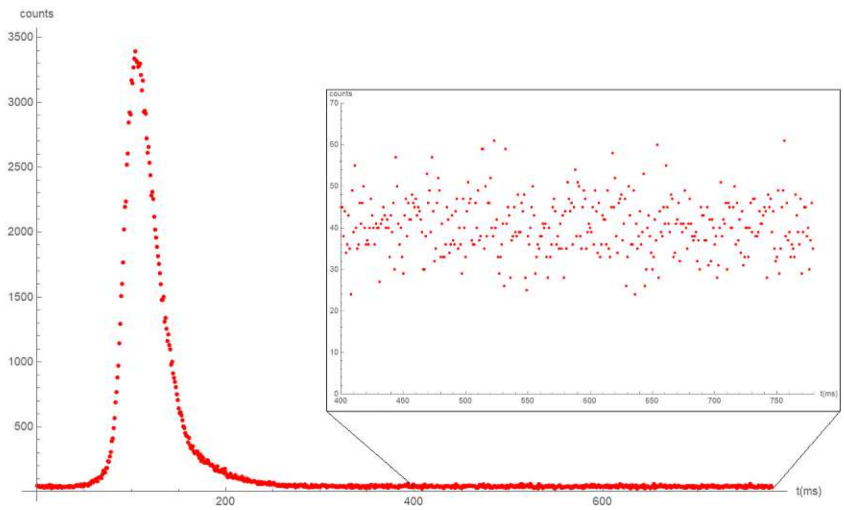

Figure 4.2: Ground measurement with all fields turned off and the chopper on, for a time of 66031 s.

We will use this measurement as an example to explain our whole process of treatment to obtain a graph displaying the rate depending on the speed of the neutrons. We first restricted the data to the time window that concerned us, *e.g.* from 50 ms ($\approx 20\,\mathrm{m.s^{-1}}$) to 360 ms ($\approx 3\,\mathrm{m.s^{-1}}$) and corrected the data to take the offset of the chopper into account. Then we normalised them to suppress the differences of the measurement times. Finally, we removed the background noise that we had in our signal: past 400 ms after the aperture of the chopper, neutrons could only have a velocity of 2.65 $m.s^{-1}$ or less, which is extremely rare. Furthermore, the zoom shows that the signal does not show any dependency on the tof past 400 ms. We averaged this noise and withdrew it from the counts for each bin. To avoid negative values, we set the standard deviation of the evaluated noise as a minimum for any value.

Then, we sorted the data by neutron velocity. We created uniform bins of 0.25 $m.s^{-1}$ and spread the counts accordingly. Obviously, for higher values of speed, some of them found themselves between two values of tof. We smoothed the data by dividing each time bin in 50 0.02 ms bins (smaller would cost too much unnecessary calculation time) and allowing them an equal 50^{th} of the counts. It yielded us the following plot.

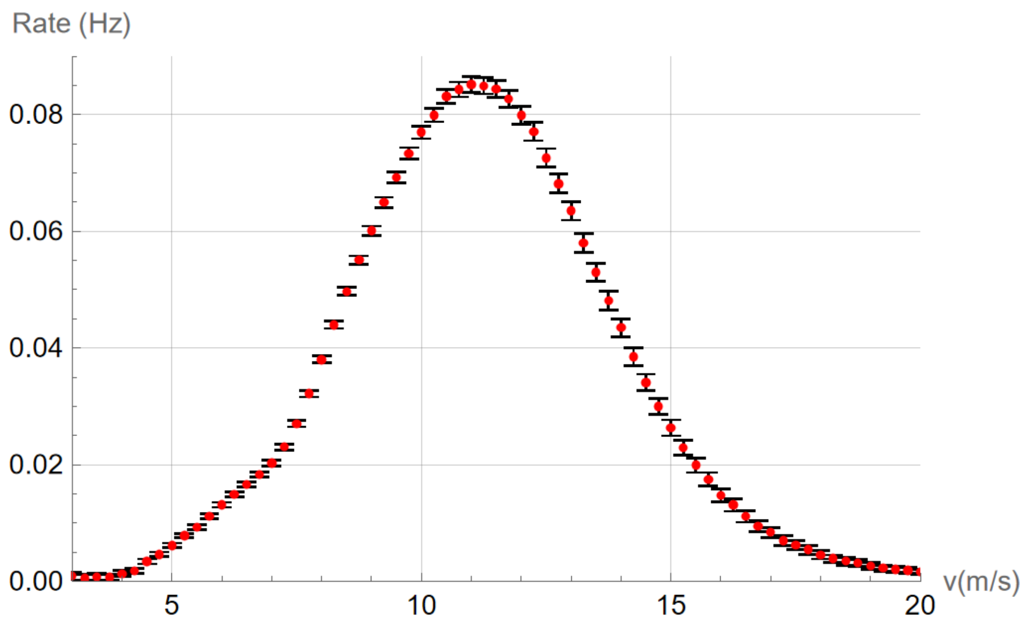

Figure 4.3: Ground measurement with all fields turned off and the chopper on, for a time of 66031±0.5 s. The standard deviation is shown by the black fences following a Poisson law.

A zoom on smaller velocities allows us to notice how big the standard errors become compared to the value themselves.

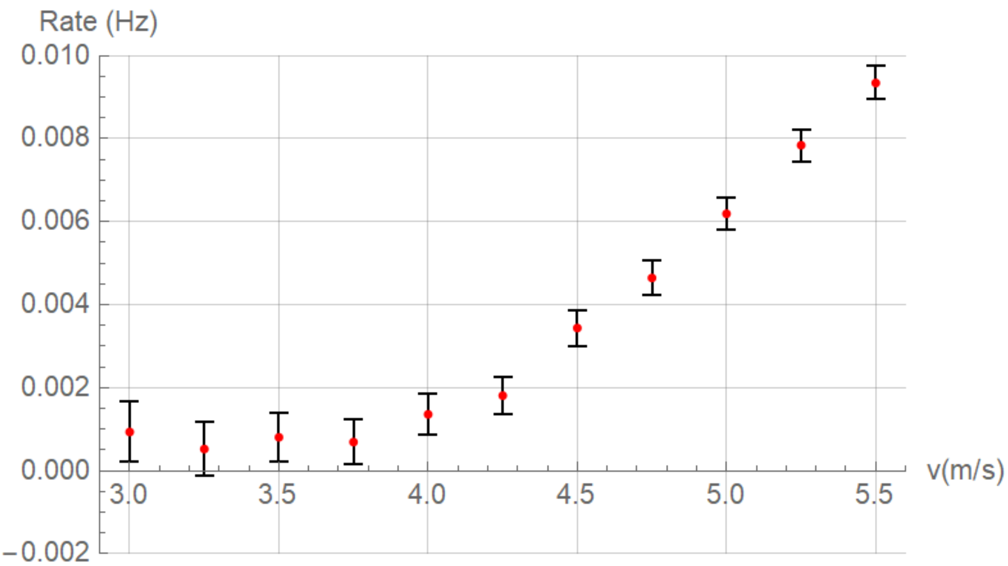

Figure 4.4: Zoom of the ground measurement for the small velocities region with standard deviations.

4.2 Polarisation efficiency

Following this method, we arranged 7 other sets of data, each corresponding to a measurements with different parameters, including the spin flipper, the nature of the foil and the magnetic fields. For the polarisation efficiency, a comparison between the measurements with or without the guiding field and the field of the detector are useful. It especially helps notice the impact of the detector foil on the polarisation.

The effect of the fields is especially notable between 5 and 8 m.s^{-1}. This is exactly the realm of the critical energy of iron, meaning that the polarisation of the detector foil caused by the magnetic field allows a significant part of the neutrons polarised in the right direction do go through it and be detected.

Below 4.5 m.s^{-1}, the neutron rate is very low and the rate difference with it. Although neutrons from 3 to 4 m.s^{-1} were theoretically in our region of interest, their rate is so low that relative differences become erratic, as is shown in the table below:

Above 11 m.s^{-1}, the relative difference is less than 1 %, showing that the polarising fields have little to no effect for velocities above that value.

The next measurement was made with the guiding field in the same direction (down), but with the field of the detector set in the other direction. Surprisingly enough, the change didn't appear to change anything to the

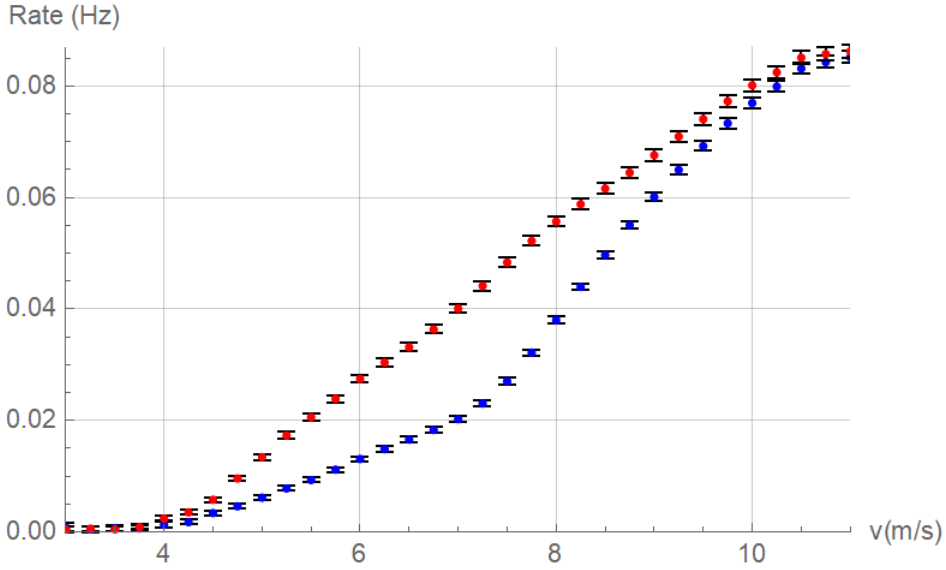

Figure 4.5: Influence of the guiding field on the neutron rate for velocities between 3 and 11 m.s^{-1}. The red curve was measured with a guiding field between 0.2 and 0.8 mT, and the field at the detector worth about 1.2 mT.

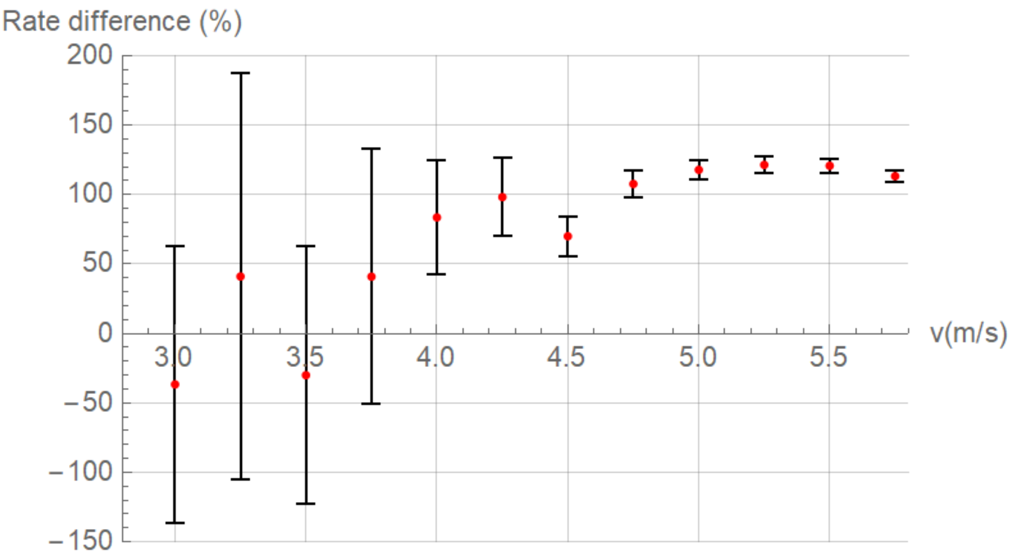

Figure 4.6: Zoom of the relative rate difference (based on the measurement without field) on the 3 to 5 m.s^{-1} region.

curve.

We also compared the data when the chosen foil was other than the initial

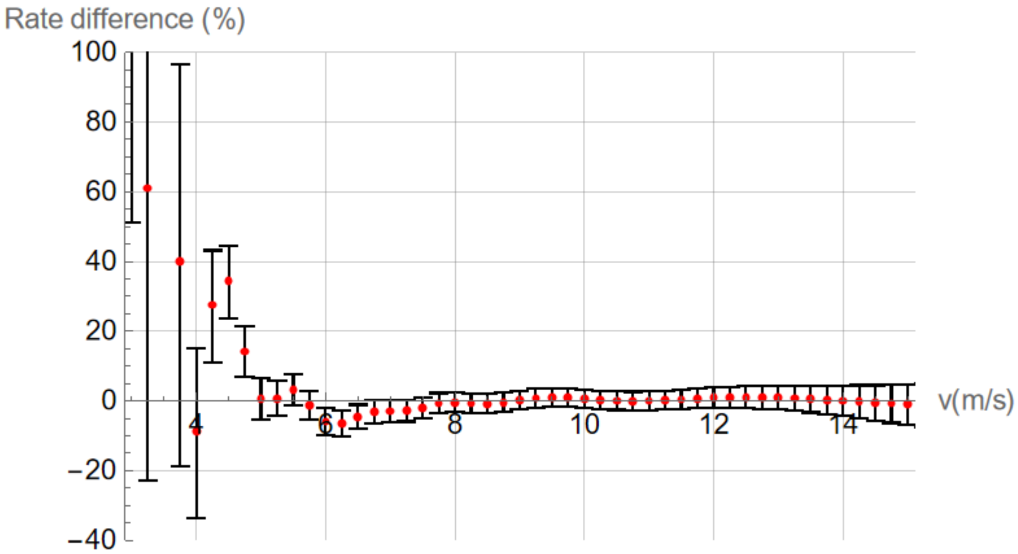

Figure 4.7: Relative rate difference between opposite polarisation of the detector, based on the measurement when the detector is down.

iron foil for the polariser: we had at our disposal another iron foil, which was scratched, and an aluminium foil. We carried out measurements with both of these foils and also one without any foil. The results are shown in the plot below:

It has proved useful to redraw these curves in accordance to the wavelength of the neutrons. The relation between velocity v and wavelength λ states that $\lambda = \frac{h}{mv}$, with h the Planck's constant $h \approx 6.626 \times 10^{-34}$ J.s and m the mass of the particle. Since we know our velocity in respect to the time and distance of flight t and d, we can write:

$$\lambda = \frac{h}{md}t$$

We can thus use this proportionality relation between time of flight and wavelength to build our plots.

The nature of the foil or its absence is noticed at highest for velocities ranging from 7 to 12 m.s^{-1}. The curve of the aluminium has the exact same shape as the curve of the "no foil" measurement, with a ratio close to constant (see 4.10), whereas the red curve displays a gentler slope between 7 and 9 m.s^{-1}.

We notice this more clearly in the figure 4.12. There is a hollow in the curve corresponding to iron in the realm of $7.5 - 9.5$ m.s^{-1} (corresponding to $40 - 50$ nm), clearly showing the higher absorption of neutrons from iron

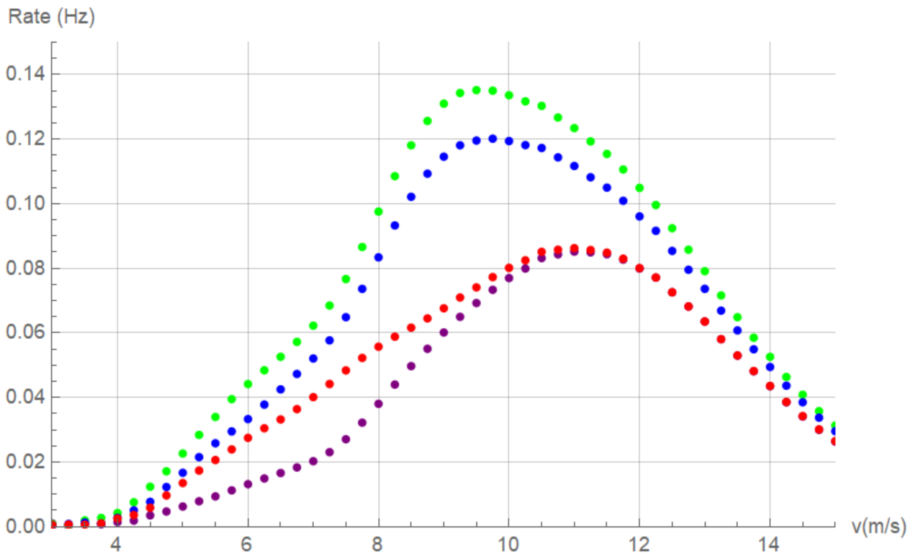

Figure 4.8: Rate for the different foils with the ground measurement shown in purple. The iron foil corresponds to the red curve, the aluminium foil to the blue one and no foil to the green one.

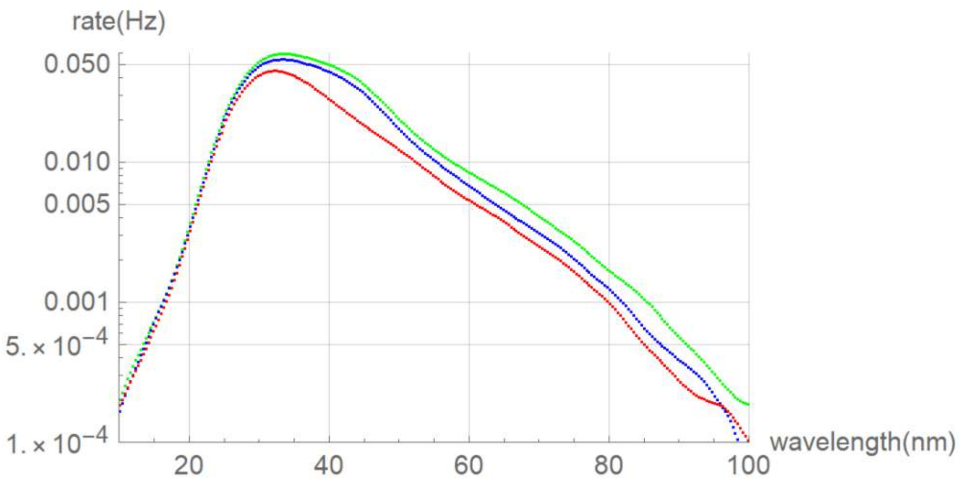

Figure 4.9: Rates of the measurements with different setups, in function of the wavelength, in a logarithmic scale. Green: no foil, Blue: Aluminium foil, Red: Iron foil.

due to its higher potential. For lower velocities, the hollow is not visible because the neutrons in the right spin direction are a lot more susceptible to get through the foil due to the lower potential of the magnetised foil, and compensate the extra absorption of neutrons.

The purple curve, showing the measurement with the spin-flipper, proves that the neutrons beam is strongly polarised for low velocities. This is confirmed by the curve of the ground measurement (without any field), for which the dropping of the rate shows the additional absorption of low velocity neutrons.

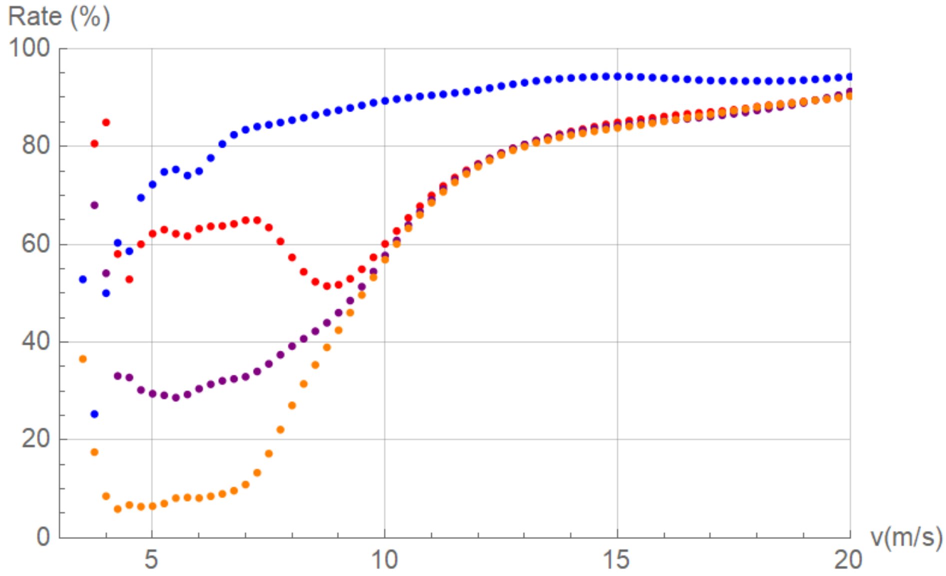

Figure 4.10: Rates of the measurements with different setups, relative to the measurement made without foil. Blue and red stand respectively for the aluminium and iron foils under standard conditions, and orange for the measurement with spin flipper.

Likewise, we build the plot with the wavelength of the incoming neutrons in abscissa, along with the transmission rate plot relatively to the rate with the measurement made with the aluminium foil.

We show in 4.13 the polarisation efficiency of the polarising installation. It must be underlined that the values displayed by the curve are necessarily inferior to the real value of polarisation efficiency, since the spin-flip efficiency is not perfect. We discuss in the next section why this makes a valid approximation.

We calculate the mean efficiency for velocities between 5 and 7 m/s:

$$P_{mean} = \frac{1}{\Delta v} \int_{5\,m/s}^{7\,m/s} P(u)\, du \approx 84.8\,\% \tag{4.1}$$

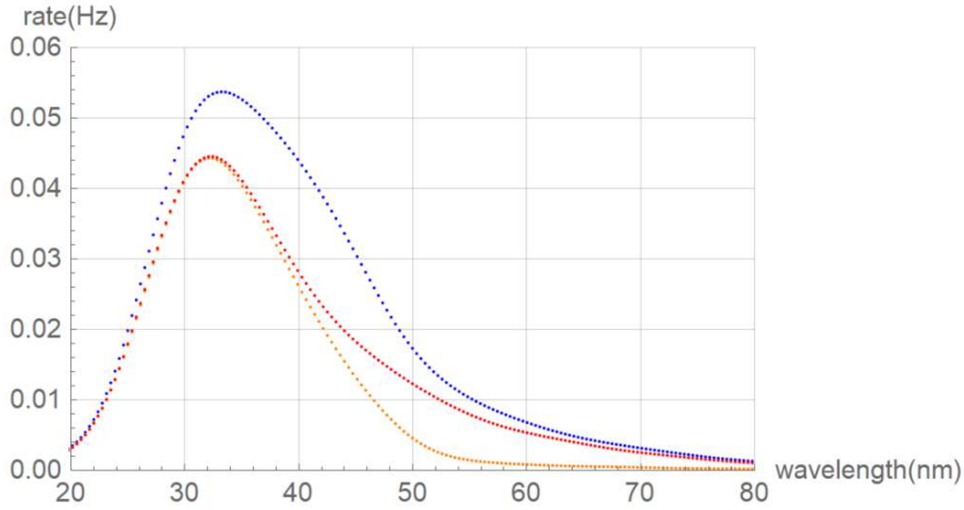

Figure 4.11: Rates of the measurements with different setups, depending on the wavelength. Blue and red stand respectively for the aluminium and iron foils under standard conditions, purple stands for the ground measurement and orange for the measurement with spin flipper.

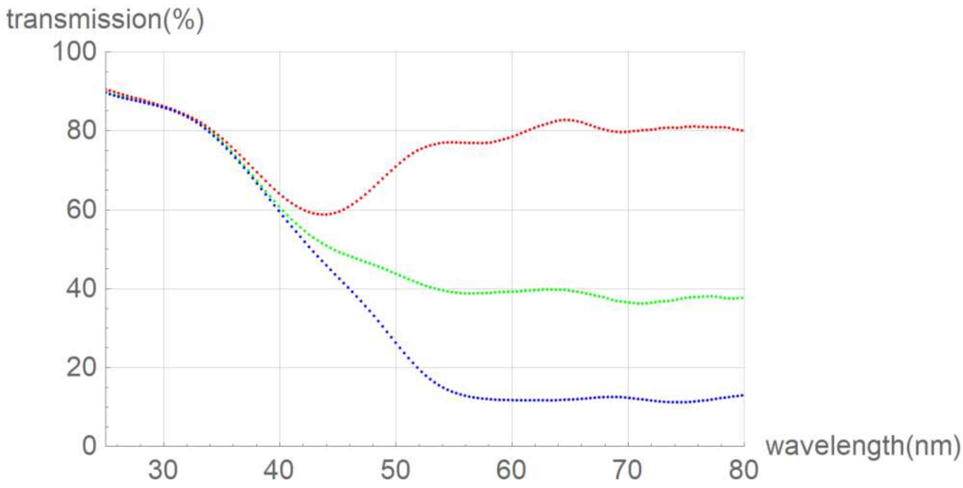

Figure 4.12: Red: fields down, Green: fields off, Blue: Spin-flipper on.

4.3 Spin-flip efficiency

The spin-flipper that we used is already depicted in the previous section. Its efficiency has first been roughly evaluated depending on the frequency delivered to the coil. As explained in 2.2, the frequency must match the Larmor frequency that corresponds to the magnetic field surrounding the

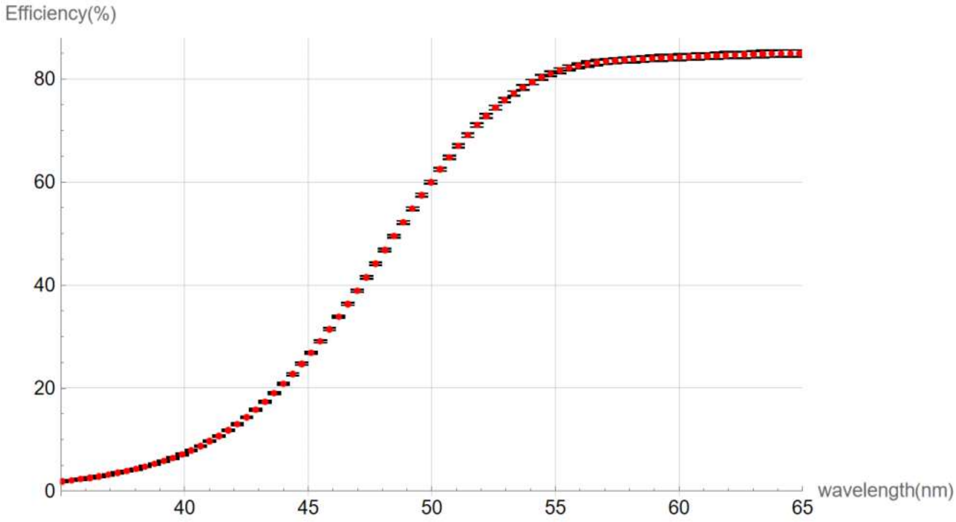

Figure 4.13: Wavelength-dependent polarisation efficiency. We cropped the wavelength that correspond to velocities from 6 to 11 m/s.

coil. As it is rather a range than a fixed value, due to the field gradient, we expected the flip to work efficiently for a frequency range as well. It is shown in [Klauser13] that the efficiency of an adiabatic spin-flip is very close to perfect for neutrons with wavelengths around 0.5 nm. Since slower neutrons, like those of our experiment, have a better adiabatic parameter, we expect the flip efficiency to be at least as good, as long as the chosen frequency lies within the adequate range.

We drove rate measurements over a short duration, but we turned off the spin flipper so that the counts would be numerous enough to determine the optimal frequency. Sorting the neutrons according to velocity was, in this qualitative measurements, not relevant.

With all fields set in *down* position and the chopper deactivated, we proceeded to a ground measurement without spin-flipper. Then, we did measurements with broad values of frequencies, ranging from 5 up to 40 kHz. For every one of these measurements, the voltage at the ends of the coil was set to be 1 V.

In accordance to the theory, the biggest change occurs for frequencies which are closer to the prediction of 15 kHz. We narrowed the optimal frequency with an additional series of measurements.

We decided to chose a frequency of 16 kHz for the remaining of the experiment. A brief series of measurements for voltages ranging from 0.2 V to 2.5 V at the ends of the coil showed that a higher voltage was profitable to the spin-flip efficiency, albeit with a limit.

Frequency	Counts	Counts per second	Relative difference
None	11714	11714	0 %
5 kHz	11706	117.06	0.0 %
10 kHz	11592	115.92	1.0 %
15 kHz	9468	94.68	19.2 %
20 kHz	9539	95.39	18.6 %
25 kHz	10802	108.02	7.8 %
30 kHz	11257	11.257	3.9 %
40 kHz	11427	114.27	2.5 %

Table 4.1: Effect of the spin flipper on the rate for various frequencies for a 100 s duration

Frequency	Counts	Counts per second	Relative difference
Reference	11714	117.14	0 %
15 kHz	9468	94.68	19.2 %
16 kHz	9334	93.34	18.6 %
17 kHz	9577	95.77	20.3 %
18 kHz	9420	94.20	19.6 %
20 kHz	9860	98.60	15.8 %

Table 4.2: 2^{nd} series of measurements for a 100 s duration

Voltage	Counts per second	Relative difference
Reference	117.14	0 %
0.213 V	115.73	1.2 %
0.640 V	104.70	10.6 %
1.254 V	94.53	19.3 %
1.720 V	94.10	19.7 %
2.461 V	96.50	17.6 %

Table 4.3: 3^{rd} series of measurements for a 50 s duration

The decrease for the higher value of voltage was interpreted as a deviation rather than a systematical decrease, because to the duration of the measurements was relatively short. We picked the last but one value of voltage (1.720 V) to be used for the rest of the experiment.

Conclusio

Summary

This thesis was mostly an experimental work, even though theoretical tasks were required, which can be found in Appendix A. Due to the Covid-19 situation, it was not clear for a long period of time when the experiment could be carried out. In regard of qBounce, our work allowed us to fully consider the possibility of a spin-dependent part in the GRS measurements. Our results were rather satisfying at this kind of setup at the Test Beam of PF2 which has a rather low neutron flux. The polarisation effect was clearly noticeable, although its quantification was complicated due to the large number of degrees of freedom in the experiment. The spin-flip was also obvious to see and very efficient, once the right frequency and the sufficient voltage were applied. Altogether, our results state that polarization and spin-flip have an efficiency which is larger than 84.8 %. We estimate the spin-flipper efficiency at close to 100 %. In the literature, that kind of spin-flipper is also considered very reliable at 100 %. With the assumption that both polarisers have an equal polarisation efficiency, the neutron polarisation is superior to 92 %.

Outlook

Further experiments concerning neutron polarisation could be carried out following the principle that we used in our experiment. It would be advised to look for more compact and stable setups that the one we built, but it might require a brand new design. A complete analysis of the incoming beam would be useful to try and get rid of a degree of freedom concerning the initial rate of the neutrons. All things considered, the design of a spin-dependent experiment could lead to exciting new results and should definitely be taken further if possible. The adjustments that it would do not seem too consequent and could give even more possibilities to qBounce and GRS in general.

Appendix A

Measurement of the mirror steps

Although our experiment requires and involves extreme care and as high precision work as possible, flaws are, in the realm of experimental science, practically impossible to fully avoid. In this particular case, the imperfection in the setup that we are interested in regards the junctions between mirrors, and possible gaps, or more precisely height differences and variations between consecutive mirrors, physically causing steps in the course of the incoming neutrons.

It was already stated that the particles interacted repulsively with the surface of the mirrors and the wave function nullified for z $\leqslant$ 0. When a particle encounters such a step, there are two different conditions for z. If s is the step between the mirrors, those conditions are:

$$\psi(z=0)=0 \quad and \quad \psi(z=s)=0 \tag{A.1}$$

At some extent, we can well imagine that this step can cause a state transition of the particle, given that its eigenenergy depends on the offset of its wave function as we discussed in the section 1.2.2. The likelihood of a state transition is mathematically given by the scalar product between the states, each one given its respective boundary condition.

We look at a particle in a state j and its possible transition to the state k. The considered eigenstates have wave functions written $\psi_{(j)}$ *and* $\psi_{(k)}$, and their scalar product can be written as follows:

$$\left\langle \psi_{(j)} \middle| \psi_{(k)} \right\rangle = \int_0^{+\infty} \psi^*_{(k)}(z-s)\psi_{(j)}(z)\,\Theta(z-s)\,dz \tag{A.2}$$

We remind that on a resting mirror with static boundary conditions, the eigenstates of the wave function are written with the help of the convergent solution of the Airy equation. This gives:

$$\psi_j(z) = Ai(\frac{z}{z_0} - AiZero_j) \tag{A.3}$$

Ai is the convergent Airy function and $AiZero_j$ is the j^{th} annihilation point of the function, starting from 0 and towards negative values ($\forall x \in \mathbb{R}_+, Ai(x) > 0$).

The probability depending on the height of the step is written as follows:

$$P(|\psi_j\rangle \rightarrow |\psi_k\rangle) = \left| \int_0^{+\infty} \psi^*_{(k)}(z-s)\psi_{(j)}(z)\,\Theta(z-s)\,dz \right|^2 \tag{A.4}$$

For our particle, the wave function must be made so that the scalar product gives a law of probability:

$$\sum_{i \geqslant j}^{+\infty} \left| \left\langle \psi_{(i)} \middle| \psi_{(j)} \right\rangle \right|^2 = 1 \tag{A.5}$$

The Heaviside step function θ is essential to respect the boundary conditions at both sides of the step.

This integral can only be approximated numerically for any other value than zero and from a state to itself, for which, an analytical solution exists. From a state to another one, when the value of the step is zero, the scalar product gives zero. This means that without a step, it is impossible for a particle to change state spontaneously. The probability of a transition is here asymmetrical. In absolute value, a negative step (downwards) of same height will result in a greater probability of a state transition. As a matter of fact, this virtually gives supplementary potential energy to the particle that has a chance to result in a state transition. For a positive step (upwards), particles can be reflected as they hit the step. They lose potential energy and have a chance to return to a more fundamental state when they encounter the step. The transition from a state j to a state k is maximal when the step respects the following condition:

$$s = \frac{E_j - E_k}{mg} \tag{A.6}$$

Series of measurements have been made by my supervisors and co-workers during the cycle n°188 (August-September 2020) that I have been provided for analysis. They include positions and angles of the consecutive mirrors and the step in between can therefore be calculated.

The data include 3 categories of measurements for each mirrors: the height z, the angle along the beam direction rot_x and the angle perpendicular to

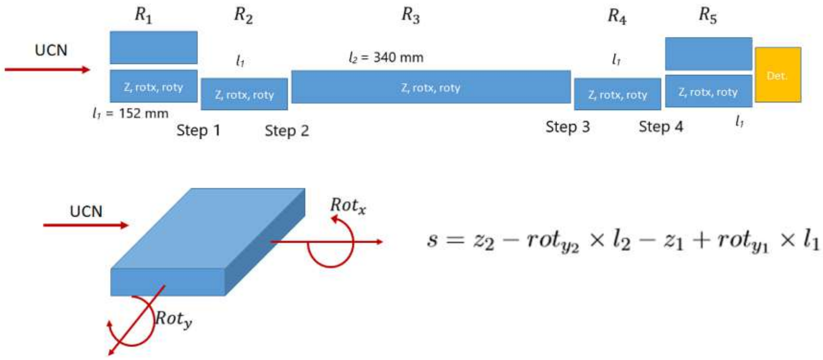

Figure A.1: Description of the problem

it rot_y. The step between two consecutive mirrors is given by the following formula, with l_1 and l_2 the respective lengths of the consecutive mirrors:

$$s = z_2 - rot_{y_2} \times l_2 - z_1 + rot_{y_1} \times l_1 \tag{A.7}$$

The length l is $340mm$ for region 3 and $152mm$ for all other regions. This is valid in the approximation of very small angles.

From there, we can calculate the scalar product corresponding to the probability of a state transition. We solely used the programming and computing tool $Mathematica$ to build up data and histograms for the step values, and the calculation of the approximated probabilities of a transition encountering the step.

Although our program is not able to provide an analytical result nor an exact answer to our scalar products in the vast majority, it is able to calculate a very fine approximation by integrating from 0 to a number large enough for the approximation to be precise, like 200: numerous tries have been made, and integrating up to 100, 200, 1000 or even 10^6 does not affect the approximation down to the 6^{th} significant digit.

According to the measurements, the step between two consecutive mirrors never exceeds $1\mu m$ (in the worst case, there are less than 0.1% values beyond $0.7\mu m$ in absolute value). This means that the entirety of our data is small compared to the typical length that we take into account in our experiment ($z_0 >> s$). We can therefore confirm that we are in the small perturbation approximation. We can thus calculate and plot a histogram of the transition probabilities.

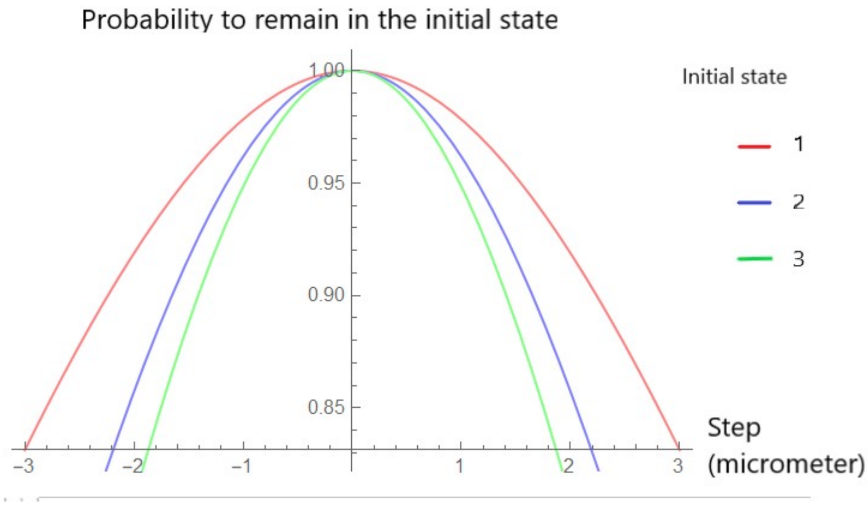

Figure A.2: The probability to stay in the 1^{st} state sinks below 0.9 for a step higher than approximately 2.4 μm

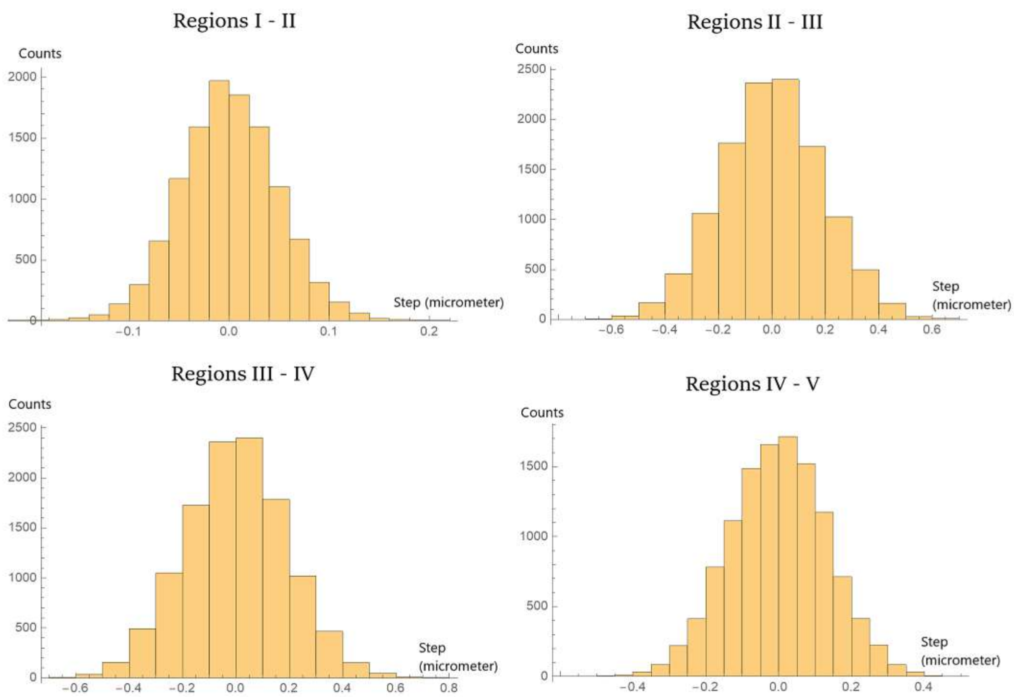

Figure A.3: The steps between every consecutive mirrors as measured during the 188^{th} cycle

Bibliography

[Ramsey50] Norman Ramsey. ‘A molecular beam resonance method with separated oscillating fields’. In: *The American Physical Society* 78.6 (1950), pp. 695–699.

[Taran75] Yu M. Taran. ‘Fast adiabatic neutron spin flip’. In: (1975).

[Golub et al.91] Robert Golub, David Richardson and Steve Lamoreaux. *Ultra-Cold Neutrons*. CRC Press, 1991.

[Phillips98] William D. Phillips. ‘Laser Cooling and Trapping of neutral Atoms’. In: *Reviews of Modern Physics* 70.3 (1998), pp. 729–734.

[Neutron Booklet03] Johnson et al. *Neutron Data Booklet*. A.-J. Dianoux and Gerry Lander, ILL, 2003, pp. 2.8–1.

[Trautman06] Andrzej Trautman. ‘Einstein-Cartan Theory’. In: *Encyclopedia of Mathematical Physics* 2 (2006), pp. 189–195.

[Seo et Al.07] P.-N. Seo et al. ‘High-Efficiency Resonant RF Spin Rotator with Broad Phase Space Acceptance for Pulsed Polarized Cold Neutron Beams’. In: *APS Physics* 11 (2007).

[Abele et al.09] Hartmut Abele et al. ‘Ramsey’s method of separated oscillating fields and its application to gravitationally induced quantum phase shifts’. In: *The American Physical Society* (2009), pp. 065019-1 –065019-8. DOI: `10.1103/PhysRevD.81.065019`.

[Cullity & Graham09] B.D. Cullity and C.D. Graham. *Introduction to Magnetic Materials*. Wiley, 2009.

[Jenke11] Tobias Jenke. ‘qBounce - vom Quantum Bouncer zur Gravitationsresonanzspektroskopie’. 2011, pp. 88, 107–109.

[Saul11] Heiko Saul. 'Weiterentwicklung des Detektor- und Auslesekonzepts für das Gravitationsexperiment qBounce'. 2011, pp. 29–33.

[Beringer et al.12] J. Beringer and Particle Data Group. 'Review of Particle Physics'. In: *Regents of the University of California* (2012). DOI: `https://doi.org/10.1103/PhysRevD.86.010001`.

[Jenke et al.13] Tobias Jenke et al. 'Ultracold neutron detectors based on 10B converters used in the qBounce experiments'. In: *Nuclear Instruments and Methods in Physics Research Section A: Accelerators, Spectrometers, Detectors and Associated Equipment* (2013). DOI: `https://doi.org/10.1016/j.nima.2013.06.024`.

[Klauser13] Christine Klauser. 'High precision neutron polarisation for PERC'. 2013, p. 66.

[Jenke et al.14] Tobias Jenke et al. 'Gravity Resonance Spectroscopy Constrains Dark Energy and Dark Matter Scenarios'. In: *American Physical Society* (2014). DOI: `https://doi.org/10.1103/PhysRevLett.112.151105`.

[Cronenberg16] Gunther Cronenberg. 'Frequency Measurements testing the Newton's gravity Law with the Rabi-qBounce experiment'. 2016, pp. 7–12, 73–77.

[Micko18] Jakob Micko. 'qBounce - Gravity Resonance and Ramsey Spectroscopy'. 2018, pp. 6–16.

[Pokotilovski18] Yu.N. Pokotilovski. 'Experiments with ultracold neutrons - first 50 years'. In: *Physics Letters B.* 483 (2018), pp. 15–22. DOI: `10.1016/s0370-2693(00)00579-7`.

[Rechberger18] Tobias Rechberger. 'Ramsey spectroscopy of gravitationally bound quantum states of Ultra-Cold Neutrons'. 2018, pp. 88, 107–109.

[Killian20] Carina Killian. 'qBounce systematic analysis of the Ramsey setup'. 2020, pp. 56–59.

[Soldner] Torsten Soldner. 'Polarization for precision measurements'. In: Institut Laue-Langevin, pp. 20–25.

List of Figures

1.1 Side view of the schematic qBounce setup 2
1.2 π-flip (red arrow) from the pure state $|0\rangle$ to the state $|1\rangle$ . . . 4
1.3 $\pi/2$-flip (red arrow) from the pure state $|0\rangle$ to a mixed state and free propagation (green arrows) 5
1.4 Potentials for the first five eigenstates interaction couples . . . 8
1.5 Transition frequencies between the first five eigenstates 8
1.6 Principle of the polarisation-detection setup 11

2.1 Field gradient in relation to the field for $\lambda = 1$ 17

3.1 Side view of the schematic setup 20
3.2 Picture of the Test-Beam Experiment. We can see the polariser surrounded by black plates, where the pipe of the vacuum pump takes the air from, then the beam going on the right, through the first and the second spin-flipper, and finally the detector, within the massive metallic frame. 21
3.3 Spectrum as shown in [Jenke et al.13] 22
3.4 Rates measured for different values of voltage for the detector foil. In red, the measurements were made with ascending voltages and in blue with descending voltages. The dashed curves represent what we qualitatively expected from the theory. 23
3.5 Aperture of the chopper after the opening signal 24
3.6 Magnetic profile of the polariser. Neutrons go through the beam from the left to the right. The foil is represented by the vertical line between the magnets. 25
3.7 Magnetic profile longitudinal to the coils, from the left to the right. 26
3.8 Magnetic profile longitudinal to the coils, from the left to the right. 27

3.9 Magnetic profile of the whole installation; the detector has a built-in polariser. Most of the values were likely underestimated because they could not be taken at the exact center (the guiding tubes and the spin-flippers were already installed). 28
3.10 Magnetic profile near the detector polarised in the *up* direction. 29

4.1 Test measurement with all fields turned off and the chopper on, for a time of 2433 s. 31
4.2 Ground measurement with all fields turned off and the chopper on, for a time of 66031 s. 31
4.3 Ground measurement with all fields turned off and the chopper on, for a time of 66031±0.5 s. The standard deviation is shown by the black fences following a Poisson law. 32
4.4 Zoom of the ground measurement for the small velocities region with standard deviations. 33
4.5 Influence of the guiding field on the neutron rate for velocities between 3 and 11 $m.s^{-1}$. The red curve was measured with a guiding field between 0.2 and 0.8 mT, and the field at the detector worth about 1.2 mT. 34
4.6 Zoom of the relative rate difference (based on the measurement without field) on the 3 to 5 $m.s^{-1}$ region. 34
4.7 Relative rate difference between opposite polarisation of the detector, based on the measurement when the detector is down. 35
4.8 Rate for the different foils with the ground measurement shown in purple. The iron foil corresponds to the red curve, the aluminium foil to the blue one and no foil to the green one. . . 36
4.9 Rates of the measurements with different setups, in function of the wavelength, in a logarithmic scale. Green: no foil, Blue: Aluminium foil, Red: Iron foil. 36
4.10 Rates of the measurements with different setups, relative to the measurement made without foil. Blue and red stand respectively for the aluminium and iron foils under standard conditions, and orange for the measurement with spin flipper. 37
4.11 Rates of the measurements with different setups, depending on the wavelength. Blue and red stand respectively for the aluminium and iron foils under standard conditions, purple stands for the ground measurement and orange for the measurement with spin flipper. 38
4.12 Red: fields down, Green: fields off, Blue: Spin-flipper on. . . . 38
4.13 Wavelength-dependent polarisation efficiency. We cropped the wavelength that correspond to velocities from 6 to 11 m/s. . . 39

A.1 Description of the problem 44
A.2 The probability to stay in the 1^{st} state sinks below 0.9 for a step higher than approximately 2.4 μm 45
A.3 The steps between every consecutive mirrors as measured during the 188^{th} cycle 45

List of Tables

4.1 Effect of the spin flipper on the rate for various frequencies for a 100 s duration 40
4.2 2^{nd} series of measurements for a 100 s duration 40
4.3 3^{rd} series of measurements for a 50 s duration 40

Acknowledgements

It is important to me to give my sincere thanks to the many yet all crucial people that helped me and supported me throughout this thesis.

I would like to thank Prof. Hartmut Abele for the supervision of my thesis, the opportunity that he gave me to work in a most exciting experiment of particle physics, and to have given many consideration to my work and my results.

I feel much obliged to Dr. Tobias Jenke for supervising me in the ILL and for allowing my internship in spite of the difficult conditions in this period, and I thank him for all the efforts made to keep my progress possible.

I give my thanks to Jakob Micko, the PhD student with whom I worked on the platform and who saw me through the experiment, gave me immeasurable help and advice, and tried to prevent my many mistakes as a green and somewhat clumsy experimenter.

I express my gratitude toward Stephanie Roccia, who made herself available to help us build and use the experiment, gave me counsel and taught me valuable things to carry out my project.

I thank Thomas Brenner for his availability on the Platform PF2 and for his help as well. He always helped solve technical issues.

I also give my regards to the staff of NPP and of the ILL in general, who made my stay at work very agreeable and helped me enjoy my days on site.

I thank Christoph, who did his project thesis at the ILL with me. Teamworking with him was very efficient and enjoyable, and his was always a welcome sight.

Finally, I give my warm thanks to my family and friends who supported me, listened to me, tried to understand and sometimes even help, and whose faith waved away my doubts and pushed me throughout my studies.

Eidesstattliche Erklärung

Hiermit versichere ich, dass ich die vorliegende Arbeit ohne Hilfe Dritter und nur mit den angegebenen Quellen und Hilfsmitteln angefertigt habe. Ich habe alle Stellen, die ich aus den Quellen wörtlich oder inhaltlich entnommen habe, als solche kenntlich gemacht. Diese Arbeit hat in gleicher oder ähnlicher Form noch keiner Prüfungsbehörde vorgelegen.

Hugo Wetter, Wien, den 30.03.2022

Wien, den 30. März 2022